UNIVERSIDADE FEDERAL DE PERNAMBUCO

CENTRO DE CIÊNCIAS EXATAS E DA NATUREZA

PROGRAMA DE PÓS-GRADUAÇÃO EM FÍSICA

ALEXSANDRO RAMOS DOS SANTOS

ELECTROMAGNETIC INTERFERENCE SHIELDING EFFECTIVENESS OF NANO AND CARBON COMPOUNDS: An analysis of yttrium-iron garnet, bacterial cellulose, nitrogen-doped reduced graphene oxide and cobalt and iron nanowires

Recife

2024

ALEXSANDRO RAMOS DOS SANTOS

ELECTROMAGNETIC INTERFERENCE SHIELDING EFFECTIVENESS OF NANO AND CARBON COMPOUNDS: An analysis of yttrium-iron garnet, bacterial cellulose, nitrogen-doped reduced graphene oxide and iron and cobalt nanowires

Dissertação apresentada ao Programa de Pós-Graduação em Física da Universidade Federal de Pernambuco, como requisito parcial para obtenção do título de mestre em Física. Área de concentração: Física da matéria condensada e de materiais.

Orientador: Eduardo Padrón Hernandez.

Recife

2024

ALEXSANDRO RAMOS DOS SANTOS

ELECTROMAGNETIC INTERFERENCE SHIELDING EFFECTIVENESS OF NANO AND CARBON COMPOUNDS:

An analysis of yttrium-iron garnet, bacterial cellulose, nitrogen-doped reduced graphene oxide and iron and cobalt nanowires

Dissertação apresentada ao Programa de Pós-Graduação em Física da Universidade Federal de Pernambuco, como requisito parcial para a obtenção do título de Mestre em Física.

Aprovado em: 29/02/2024.

BANCA EXAMINADORA

_____
Prof. Dr. Eduardo Padrón Hernández
Orientador
Universidade Federal de Pernambuco

_____
Prof. Dr. Antonio Azevedo da Costa
Examinador Interno
Universidade Federal de Pernambuco

_____
Prof. Dr. João Maria Soares
Examinador Externo
Universidade do Estado do Rio Grande do Norte

AGRADECIMENTOS

Agradeço primeiramente à minha família, sem ela eu não conseguiria estar aqui. Agradeço à minha mãe, Dona Alexandra, que com muito esforço conseguiu colocar ambos filhos em universidades. Agradeço ao meu pai, Seu Pedro, que enfrentou batalhas difíceis para que eu possa ter chegado aqui. Agradeço à minha avó, Dona Claudinete, uma guerreira, e ao meu avô Seu Antônio, que infelizmente nos deixou durante esse último semestre do mestrado. Agradeço também aos meus irmãos, em especial Patrícia e aos meus tios, tias e primos, que muito me apoiaram para que eu pudesse chegar aqui.

Agradeço segundamente aos meus colegas do laboratório do MESOMAG, que em muitos momentos de dificuldade foram por mim. Meu orientador, Professor Eduardo Padrón, ao grupo que esteve pesquisando em blindagem, Adriana, Samuel, Emanoel Laurertan, Pedro, Thais, Dyego, Lilian, Gisele. Agradeço também aos outros membros de nossa equipe, Marcos, Daylane, Matheus Fairbancks, Filipe, Wemerson, Jean, Griselda, Willian Bocanegra, entre muitos outros que fazem, fizeram e irão fazer ciência acontecer independente de quaisquer empecilhos.

Terceiramente, agradeço às pessoas que fazem os meus dias mais leves. Agradeço à minha companheira Isabel, que muito acrescentou em minha vida, trazendo mais alegria, paz, amor, carinho entre muitas outras coisas. Agradeço aos meus amigos, o já citado Willian, ao grupo dos jubilados em física, Edilson Eugenio, Francisco Tavares e Marvin Miguel. Agradeço ao grupo dos parceiros do amor, a já citada Daylane, Fernanda, Gedeone, Joana, João Victor Cardoso, Larissa Bourbon, Luiz Matheus, Marcela Gouvêa, Mariana Odon, Matheus Duclerc e Yuri. Agradeço também aos outros amigos que passaram pelo meu caminho, Mariana, Raquel, Thiago Melo, Lucas Guilhermino, Nathália Ferino, Mayara, Brenda, Estela, Guilherme, Rafael, Lucas Alves, Yasmin, Alex Ramos, Jade, João Matheus, Maryane, Ivys, Cibbele e Ivi. Também gostaria de agradecer aos meus amigos virtuais, Maria Eduarda, Lorrane, Gabriel e Erica Alessandra, entre outros, vocês são show.

Por fim, gostaria de agradecer aos órgãos de fomento CNPQ, CAPES, FACEPE, FINEP e ao departamento de física da UFPE, seus funcionários e amigos. Sem o apoio de vocês tudo isso não seria possível numa era onde a ciência vem sofrendo severos ataques no país.

ABSTRACT

This work aims to present a possible solution to the growing problem of electromagnetic pollution through the shielding effect against electromagnetic interference, analyzed in five compounds. The methodology consists of creating a theoretical introduction to electromagnetic waves, establishing a theoretical framework for a better understanding of the electromagnetic pollution problem and the shielding effect against electromagnetic interference. It involves understanding and citing the devices causing this pollution, preparing samples of yttrium-iron garnet on alumina membrane using the sol-gel method, bacterial cellulose samples cultivated in HS medium, reduced graphene oxide samples doped with nitrogen using the Hummers method, and iron and cobalt nanowires samples with a thin layer of gold, grown on alumina membrane using the electrodeposition method to serve as potential solutions to the problem. Finally, a Vector Network Analyzer is used to measure the shielding obtained from these samples on the microwave band X. It was then observed an insignificant residual shielding for yttrium-iron garnet, low shielding in the range of 5.7 dB for bacterial cellulose, and moderate shielding for the other composites, with nitrogen doped graphene oxide with Fe_3O_4 having 27.3 dB of shielding, cobalt nanowires with 17.9 dB, and iron nanowires with 34.0 dB of shielding.

Keywords: electromagnetic shielding; microwave; yttrium-iron garnet; bacterial cellulose; reduced graphene oxide; nanowires.

RESUMO

Este trabalho tem por finalidade apresentar uma possível solução para o crescente problema da poluição eletromagnética através do efeito de blindagem contra interferência eletromagnética, analisado em cinco compostos. A metodologia consiste em criar uma introdução teórica sobre ondas eletromagnéticas, criar um arcabouço teórico para melhor compreensão do problema da poluição eletromagnética e o efeito de blindagem contra interferência eletromagnética, compreender e citar os dispositivos causadores dessa poluição, preparar amostras de granada de ítrio-ferro sobre membrana de alumina utilizando o método sol-gel, amostras de celulose bacteriana cultivadas em meio HS, amostras de óxido de grafeno reduzido dopado com nitrogênio utilizando o método de Hummers e amostras de nanofios de ferro e nanofios de cobalto com uma fina camada de ouro, crescidos sobre membrana de alumina utilizando o método de eletrodeposição para servir de potenciais soluções para o problema, por fim utilizar um *Vector Network Analyzer* para medir a blindagem obtidas dessas amostras na banda X de frequências de microondas. Foi então constatado uma blindagem residual inexpressiva para a granada de ítrio-ferro, uma blindagem baixa na faixa de 5,7 dB para a celulose bacteriana e uma blindagem moderada para os demais compósitos, sendo o óxido de grafeno dopado com nitrogênio e Fe_3O_4 com 27,3 dB de blindagem, os nanofios de cobalto com blindagem de 17,9 dB e os nanofios de ferro com blindagem de 34,0 dB.

Palavras-chave: blindagem eletromagnética; microondas; granada de ítrio-ferro; celulose bacteriana; óxido de grafeno reduzido; nanofios.

LIST OF FIGURES

LIST OF TABLES

LIST OF SYMBOLS

Symbol	Description
$\vec{\nabla} \cdot$	Divergence
$\vec{\nabla} \times$	Cross product
∇^2	Laplacian
$\vec{E}$	Electric field
$\vec{B}$	Magnetic field
ρ	Charge density
$\vec{J}$	Volume current density
μ_0	Free space permeability
ϵ_0	Free space permittivity
q	Charge
$\vec{v}$	Velocity
$\vec{F}$	Force
$\vec{D}$	Electric displacement
$\vec{H}$	Magnetic intensity
ρ_f	Free charge density
$\vec{J}_f$	Free volume current density
$\parallel$	Parallel
$\perp$	Perpendicular
$\hat{n}$	normal vector
$\vec{K}_f$	Free superficial current density
σ_f	Free superficial charge density

$\vec{X}_a$	Field X on the above portion
$\vec{X}_b$	Field X on the below portion
$\overleftrightarrow{\epsilon}$	Permittivity tensor
$\overleftrightarrow{\mu}$	Permeability tensor
ϵ	Permittivity on media
μ	Permeability on media
c	Light speed
n	Index reflection
W_E	Energy stored on the electric field
W_M	Energy stored on the magnetic field
dv	Differential volume element
u	Energy density
$\vec{S}$	Poynting vector
A	Absorption coefficient
R	Reflection coefficient
M	Multiple internal reflections coefficient
T	Transmission coefficient
X_{inc}	Incident X
X_{trans}	Transmitted X
X_{mir}	Multiple internal reflections X
X_{abs}	Absorbed X
X_{ref}	Reflected X
P	Power
ϵ_r	Relative permittivity
σ	Conductivity

ω	Angular frequency
μ_r	Relative permeability
$\vec{M}$	Intrinsic magnetization
ϵ'	The real part of permittivity
ϵ''	The imaginary part of permittivity
μ'	The real part of permeability
μ''	The imaginary part of permeability
$tan(\delta_m)$	Magnetic tangent loss.
A_X	A field in X direction
A_Y	A field in Y direction
A_Z	A field in Z direction
k_c	Cut Off wavenumber
f	Frequency
A_T	Tangential field
S	Scattering matrix
SE_T	Total Shielding effectiveness
SE_R	Shielding effectiveness due to reflection
SE_A	Shielding effectiveness due to absorption
SE_M	Shielding effectiveness due to multiple internal reflection
S_{11}	Input reflection coefficient
S_{12}	Reverse transmission coefficient
S_{21}	Forward transmission coefficient
S_{22}	Reverse reflection coefficient

LIST OF ACRONYMS

1D	One-dimension
2D	Two-dimension
2G	Second generation
3D	Three dimension
3G	Third generation
4G	Fourth generation
4.5G	4.5th generation
AR	Aspect ratio
BC	Bacterial Cellulose
BP	Buckypaper
CMC	Carboxymethyl cellulose
CNT	Carbon nanotube
COMAG	Coprecipitation of magnetite *in situ*
dB	Decibel
EM	Electromagnetic
EMI	Electromagnetic interference
EVA	Ethylene-vinyl acetate
GO	Graphene oxide
GPS	Global positioning systems
LYO	Lyophilized
MAG	Magnetite *ex situ*
MW	Microwave
NP	Nanoparticle
NPCIAMB	*Núcleo de Pesquisas e Ciências ambientais e Biotecnologia*
NrGO	Nitrogen-doped reduced graphene oxide
NW	Nanowire

PBC	Processed bacterial cellulose
PEDOT:PSS	Polystyrene sulfonate
RADAR	Radio Detection and Ranging Systems
RF	Radiofrequency
rGO	Reduced graphene oxide
S-parameter	Scattering Parameter
SE	Shielding effectiveness
SEM	Scanning electron microscopy
SrGO	Sulfur-doped reduced graphene oxide
TE	Transverse electric
TE	Transverse magnetic
UFPE	*Universidade federal de pernambuco*
UNICAP	*Universidade Católica de Pernambuco*
VNA	Vector network analyzer
WHO	World Health Organization
WPU	Waterborne polyurethane
XDR	X-Ray diffraction
YIG	Yttrium-iron garnet

CONTENTS

1 INTRODUCTION

Moore (1965) noticed an exponential growth of electronic devices, impulsing the world to a new era where communication, military technology, health processes, and even leisure are deeply connected with these devices, Newzoo (2021) noticed that exists more than 4.6 billion of smartphones all over the world in 2021, and projected the number for over 5.3 billion in 2024.

To process the increasing amount of data per second on communication, it is necessary to achieve frequencies even higher than before. Mariappan *et al.* (2016) and Ulaby (2014) say that devices that use the 2G wireless system utilize frequencies in the range of 0.9 GHz, while 3G uses frequencies around 2.1 GHz, 4G, and 4.5G can access frequencies of 2.5 GHz and most recently 5G can reach frequencies over 3.5 GHz. Meanwhile, military technology like Radio Detection and Ranging Systems (Radar), satellites, Global Positioning Systems (GPS), and drones work with frequencies around 1-8 GHz.

The World Health Organization (WHO, 2016) says that electronic devices, humans, animals in general, and the environment are constantly in contact with an increasing amount of electromagnetic power (energy per time) due to the mentioned growth of the range of frequencies and intensity used for the electric devices. These electromagnetic waves that permeate the air are the cause of a new kind of phenomenon called electromagnetic pollution (AHMAD *et al.*, 2023).

Once the energy of an electromagnetic wave increases with its frequency, higher frequencies represent a higher risk for the systems affected by electromagnetic waves. Wanasinghe and Aslani (2019) cite that "electromagnetic pollution can cause disruptions to the functionality in electronic devices and adverse effects on infants brain development and in some cases, could lead to carcinogenic conditions" and harm the environment, while The World Health Organization (WHO, 2020) says that frequencies over the microwave spectrum can be ionizing and irremediable for living beings and can make irreversible damage to the environment.

This work aims to find methods of solving the upcoming problem of electromagnetic pollution, searching for compounds that could typically be used for shielding electromagnetic pollution by measuring their electromagnetic interference shielding effectiveness.

Sun *et al.* (2024) mention that a great shielding material can be achieved by good conductors, because its high reflectance can lead to a small skin depth, that prevents the wave from penetrating through the shielded medium, whilst Ryu *et al.* (2022) say that a good potential shield is led by materials that could absorb well the electromagnetic waves, like high thermal conductivity (or high heat capacity) materials. Pai *et al.* (2022) say that the research on electromagnetic interference shielding grows by year.

Akram *et al.* (2023) describe that metals, like silver, gold, copper, iron, and many others have reasonable values for electromagnetic shielding, and semiconductors like silicon have great shielding processes. Meanwhile, Das, M., Sethy, and Sundaray (2023), say that most metals represent a second kind of electromagnetic pollution, once that most of their shielding is formed by their characteristic of reflecting the waves. Yazdi *et al.* (2020) suggest that it is necessary to find more environmentally friend-like materials for shielding and declare that organic materials could be a possible tool for this task. Wang, X. et al. (2023) suggest that magnetic materials gave an increase in the absorption shield. Feng *et al*. (2023), Qi *et al.* (2021), Verma *et al*. (2023), Erdogan *et al.* (2020), and Vu *et al.* (2021) tested on carbon-based materials for shielding and discovered that its shielding is mostly due absorption, a great characteristic for solving the secondary source of pollution, caused by metallic shields.

Electromagnetic shielding is a necessity for the upcoming years, Takahari *et al.* (2023) cite a fatality caused by electromagnetic interference pollution, and Wang, Y. H. and Li (2024) argue that this kind of pollution can be mostly reduced by the great capacity of the shields. So searching for the best system of protection and shielding is not only helpful but fundamental for future societies.

For a deep comprehension of the theme, this article foresees a theoretical and practical resource material for electromagnetic interference shielding effectiveness. The second chapter introduces the theoretical information needed for the understanding of the topic studied here, it starts by giving a brief explanation of the electromagnetic waves, from Maxwell's equations to energy conservation and the shielding effect. It gives a brief understanding of the microwave systems that will be studied in the next sections as long as it explains the equipment used for the measurements, like waveguides and the vector network analyzer and finally, it explains the experiment itself. Meanwhile the third chapter is dedicated to the

process of creating and characterizing the composites that the experiments will achieve the shielding from. Finally, the fourth chapter depicts the values obtained from the shielding of each material as far as it gives a discussion on how the values are depicted with the security standards for shielding. This work also brings a conclusion to all the processes in the fifth chapter and shows the perspectives for the next projects.

2 ELECTROMAGNETIC INTERFERENCE SHIELDING EFFECTIVENESS THEORY IN MICROWAVE SYSTEMS

The beginning of the discussion of electromagnetic interference shielding effectiveness (EMI SE) in microwave (MW) systems starts with the a priori concept of electromagnetic waves and how they propagate over the media of different materials, such as metallic and semi metallic compounds, alloys and organic matter, over a wide range of frequencies (specific ranges will be nominated as MW bands, and their classification, in addition with the equipment and technical specifications will be studied in this chapter).

2.1 ELECTROMAGNETIC WAVES

To appreciate the significance of electromagnetic waves, it is essential to delve into the historical context of their discovery and exploration. From James Clerk Maxwell's groundbreaking equations in the 19th century to the experimental validation by Heinrich Hertz, the journey to understanding the unified nature of electricity and magnetism has been one of the most captivating narratives in the history of physics.

Pozar (2012) says that fundamental to the study of electromagnetic waves are Maxwell's equations, which eloquently describe the interplay between electric and magnetic fields. Zangwill (2012) explains that these equations not only provided a theoretical framework for the existence of electromagnetic waves but also paved the way for the realization that light itself is a form of electromagnetic radiation. As can be seen in Griffiths (2017) the electromagnetic spectrum, a continuum of wavelengths and frequencies, extends from radio waves to microwaves, infrared, visible light, ultraviolet, X-rays, and gamma rays. Each segment of the spectrum offers unique insights into the behavior of electromagnetic waves.

By this way, understanding electromagnetic waves involves exploring their wave-like properties, such as wavelength and frequency. This chapter will dive into the mathematical representations of these properties and their significance in describing the nature of electromagnetic radiation.

2.1.1 Maxwell's Equations

The four equations named for Maxwell, and later depicted as how it is seen on the contemporary days, describe the behavior of electromagnetic fields. Griffiths (2017, p.337) shows that in free space the electromagnetic fields are written as equations 2.1-2.4. The first one is named as Gauss's law, and describes how the electric field behaves in the presence of a charge density. The second one does not have a specific name, but it shows the inexistence of magnetic charge density. The third one, named Faraday's law, describes how the curl of the electric field varies with the time derivative of the magnetic field. The fourth, and last one, is named as Ampere's law and has the correction imposed by Maxwell later on, where it shows how the curl of the magnetic field depends on the electrical current density and the variation on the electrical field.

$$\vec{\nabla} \cdot \vec{E} \;=\; \frac{\rho}{\epsilon_0} \tag{2.1}$$

$$\vec{\nabla} \cdot \vec{B} \;=\; 0 \tag{2.2}$$

$$\vec{\nabla} \times \vec{E} \;=\; -\frac{\partial \vec{B}}{\partial t} \tag{2.3}$$

$$\vec{\nabla} \times \vec{B} \;=\; \mu_0 \vec{J} + \mu_0 \epsilon_0 \frac{\partial \vec{E}}{\partial t} \tag{2.4}$$

Where $\vec{E}$ and $\vec{B}$ are respectively the electric and magnetic fields. ρ and $\vec{J}$, are the sources, respectively the charge density and the volume current density. While ϵ_0 and μ_0 are the free space permittivity and permeability. With the Lorentz force law (equation 2.5), the laws above describe the entire set of classical electromagnetism on free space. On the Lorentz force law, q is the charge and $\vec{v}$ and $\vec{F}$ are the velocity and the force of the electric particle.

$$\vec{F} \;=\; q\vec{E} \;+\; q\vec{v} \times \vec{B} \tag{2.5}$$

Griffiths (2017, p.341) also shows that In the media appear new entities that rule electromagnetic phenomena. The electric displacement ($\vec{D}$), that appears on dielectric media. And the magnetic intensity ($\vec{H}$), that appears on magnetized material. In terms of $\vec{D}$ and $\vec{H}$, the Maxwell's laws on media become:

$$\vec{\nabla} \cdot \vec{D} \;=\; \rho_f \tag{2.6}$$

$$\vec{\nabla} \cdot \vec{B} \;=\; 0 \tag{2.7}$$

$$\vec{\nabla} \times \vec{E} \;=\; -\frac{\partial \vec{B}}{\partial t} \tag{2.8}$$

$$\vec{\nabla} \times \vec{H} \;=\; \vec{J}_f + \frac{\partial \vec{D}}{\partial t} \tag{2.9}$$

Where ρ_f and $\vec{J}_f$ are the free sources. The free charge density and the free volume current density, respectively. The boundary conditions are also depicted by Griffiths (2017, p.342) as from equation 2.10 to 2.13, where $\parallel$ and $\perp$ the parallel and perpendicular portion of each field with respect to the normal versor ($\hat{n}$), respectively, and a and b denote above and below the surface parallel to the normal versor. $\vec{K}_f$ represents the free surface current density, while σ_f represents the free surface charge density.

$$\vec{E}_a^{\parallel} \;=\; \vec{E}_b^{\parallel} \tag{2.10}$$

$$\vec{H}_a^{\parallel} \;=\; \vec{H}_b^{\parallel} + \vec{K}_f \times \hat{n} \tag{2.11}$$

$$\vec{B}_a^{\perp} \;=\; \vec{B}_b^{\perp} \tag{2.12}$$

$$\vec{D}_a^{\perp} \;=\; \vec{D}_b^{\perp} + \sigma_f \tag{2.13}$$

Pozar (2012, p.11-12) shows that in linear media, the media permittivity and permeability can be expressed in terms of tensor algebra, as written in equations

2.14 to 2.17. The tensors appear due to the possibility of anisotropy of the media. In linear isotropic media, the equations above mentioned result in a clearer and more familiar simplification shown in equations 2.18 and 2.19.

$$\vec{D} = \overleftrightarrow{\epsilon}\,\vec{E} \tag{2.14}$$

$$\begin{bmatrix} D_1 \\ D_2 \\ D_3 \end{bmatrix} = \begin{bmatrix} \epsilon_{11} & \epsilon_{12} & \epsilon_{13} \\ \epsilon_{21} & \epsilon_{22} & \epsilon_{23} \\ \epsilon_{31} & \epsilon_{32} & \epsilon_{33} \end{bmatrix} \begin{bmatrix} E_1 \\ E_2 \\ E_3 \end{bmatrix} \tag{2.15}$$

$$\vec{B} = \overleftrightarrow{\mu}\,\vec{H} \tag{2.16}$$

$$\begin{bmatrix} B_1 \\ B_2 \\ B_3 \end{bmatrix} = \begin{bmatrix} \mu_{11} & \mu_{12} & \mu_{13} \\ \mu_{21} & \mu_{22} & \mu_{23} \\ \mu_{31} & \mu_{23} & \mu_{33} \end{bmatrix} \begin{bmatrix} H_1 \\ H_2 \\ H_3 \end{bmatrix} \tag{2.17}$$

The tensors $\overleftrightarrow{\epsilon}$ and $\overleftrightarrow{\mu}$ represent the permittivity and permeability tensor respectively, they get reduced to their respective diagonal form with only ϵ and μ on their diagonal on linear isotropic media. A priori, ϵ and μ can be complex on dispersive media or variate with the frequency while on the microwave spectrum. These media will be studied further on this chapter.

$$\vec{D} = \epsilon\,\vec{E} \tag{2.18}$$

$$\vec{B} = \mu\,\vec{H} \tag{2.19}$$

2.1.2 Wave Equation

At the heart of electromagnetic wave theory lies the wave equation, a mathematical expression derived from Maxwell's equations. These equations, formulated by Maxwell (1865) in another formulation, elegantly describe the fundamental principles governing the interplay between electric and magnetic fields. This section will guide the readers through the steps of deriving the wave equation from Maxwell's equations, emphasizing the seamless integration of these principles into a cohesive framework for understanding wave propagation

Boyce, DiPrima and Maede (2022, p. 516-518) say that the electromagnetic wave equation is a partial differential equation that characterizes the spatial and

temporal evolution of electric and magnetic fields. Solving the wave equation unveils the solutions that describe the behavior of electromagnetic waves. Plane waves, spherical waves, and other solutions play a vital role in comprehending the diverse manifestations of electromagnetic radiation. Through illustrative examples, this section will show how these solutions contribute to our understanding of wave phenomena in different contexts.

Maxwell's equations on free space without the presence of sources can be directly taken from equations 2.1 to 2.4, making $\rho = 0$ and $\vec{J} = 0$. One must obtain such coupled equations:

$$\vec{\nabla} \cdot \vec{E} \ = \ 0 \tag{2.20}$$

$$\vec{\nabla} \cdot \vec{B} \ = \ 0 \tag{2.21}$$

$$\vec{\nabla} \times \vec{E} \ = \ -\frac{\partial \vec{B}}{\partial t} \tag{2.22}$$

$$\vec{\nabla} \times \vec{B} \ = \ \mu_0 \epsilon_0 \frac{\partial \vec{E}}{\partial t} \tag{2.23}$$

Griffiths (2017, p.393-394) shows that applying the curl on the equations 2.22 and 2.23, and using the well known algebraic identity of the curl of a curl of any kind of vector $(\vec{\nabla} \times \vec{\nabla} \times \vec{A} \ = \ \vec{\nabla}(\vec{\nabla} \cdot \vec{A}) - (\vec{\nabla} \cdot \vec{\nabla}) \vec{A})$, one can obtain:

$$\vec{\nabla} \times \vec{\nabla} \times \vec{E} \ = \vec{\nabla} \times (-\frac{\partial \vec{B}}{\partial t}) \ = \vec{\nabla}(\vec{\nabla} \cdot \vec{E}) - (\vec{\nabla} \cdot \vec{\nabla}) \vec{E} =$$

$$= 0 - \frac{\partial}{\partial t}\vec{\nabla} \times \vec{B} =- \mu_0 \epsilon_0 \frac{\partial^2 \vec{E}}{\partial t^2} \tag{2.24}$$

$$\vec{\nabla} \times \vec{\nabla} \times \vec{B} \ = \vec{\nabla} \times (\mu_0 \epsilon_0 \frac{\partial \vec{E}}{\partial t}) \ \vec{\nabla}(\vec{\nabla} \cdot \vec{B}) - (\vec{\nabla} \cdot \vec{\nabla}) \vec{B} \ =$$

$$= 0 - \mu_0 \epsilon_0 \frac{\partial}{\partial t}\vec{\nabla} \times \vec{E} =- \mu_0 \epsilon_0 \frac{\partial^2 \vec{B}}{\partial t^2} \tag{2.25}$$

Since $\vec{\nabla} \cdot \vec{E} \ = \ 0$ and $\vec{\nabla} \cdot \vec{B} \ = \ 0$. Both equations got decoupled on the form: $(\vec{\nabla} \cdot \vec{\nabla}) \vec{A} = \mu_0 \epsilon_0 \frac{\partial^2 \vec{A}}{\partial t^2}$. The operator $(\vec{\nabla} \cdot \vec{\nabla})$ is sometimes denominated Laplacian or

laplace operator and often is written as ∇^2. The partial equation denominated as $\nabla^2 \vec{A} = \frac{1}{c^2} \frac{\partial}{\partial t^2} \vec{A}$ is called the wave equation, and c is the propagation speed of the wave. On this way, it is visible that both, the electric and magnetic fields represent, on free space, a wave with speed of $c = \frac{1}{\sqrt{\mu_0 \epsilon_0}}$, known as the speed of light on the free space (c = 299792458 m/s). Thus the light itself is an electromagnetic wave.

Zangwill (2012, p.585) shows that similarly, on a linear and isotropic lossless media without any free sources, the Maxwell's equations will behave the same, with a correction of the speed for $|\vec{v}| = \frac{1}{\sqrt{\mu \epsilon}}$, as follow:

$$\vec{\nabla} \cdot \vec{D} = 0 \tag{2.26}$$

$$\vec{\nabla} \cdot \vec{B} = 0 \tag{2.27}$$

$$\vec{\nabla} \times \frac{1}{\epsilon}\vec{D} = -\mu \frac{\partial \vec{H}}{\partial t} \tag{2.28}$$

$$\vec{\nabla} \times \vec{H} = \frac{\partial \vec{D}}{\partial t} \tag{2.29}$$

It is seen from a comparison of equations 2.26-2.29 with equations 2.20-2.23 that the light speed on media is smaller of the light speed on the free space by a factor of $\frac{\sqrt{\mu \epsilon}}{\sqrt{\mu_0 \epsilon_0}}$, named the reflection index (n). Thus in the media, v = c/n.

2.1.3 Energy Conservation and Power

The study of electromagnetic waves extends beyond their fundamental properties and encompasses crucial considerations related to energy conservation and power transmission. This section addresses the intricate relationship between electromagnetic waves and the conservation of energy, shedding light on the mechanisms governing energy flow, power distribution, and the practical implications of these principles across diverse applications.

Griffiths (2017, p. 357-359) discusses the partition of energy led by the particles, and as is going to be shown sooner, as like particles, fields also carry

energy. The time average energy stored on the electric (W_E) and magnetic fields (W_M) are:

$$W_E = \frac{1}{2} \int_{all\ space} \vec{D} \cdot \vec{E}\ dv \tag{2.30}$$

$$W_M = \frac{1}{2} \int_{all\ space} \vec{H} \cdot \vec{B}\ dv \tag{2.31}$$

Where v is the volume where the fields are. Which in linear, homogeneous, isotropic and lossless media, become:

$$W_E = \frac{\epsilon}{2} \int_{all\ space} |E|^2\ dv \tag{2.32}$$

$$W_M = \frac{1}{2\mu} \int_{all\ space} |B|^2\ dv \tag{2.33}$$

Griffiths (2017, p.357) reaches relations of how the summation of the equations 2.32 and 2.33 do not represent conservation of energy per time unity (power) and makes the appearance of a new term on these equations, the Poynting vector, as depicted on the equations 2.34 to 2.37.

$$\frac{d}{dt}W = \frac{1}{2} \int_{all\ space} \vec{J} \cdot \vec{E}\ dv \tag{2.34}$$

$$\vec{E} \cdot \vec{J} = -\frac{1}{2}\frac{\partial}{\partial t}\left(\epsilon_0 |E|^2 + \frac{1}{\mu_0}|B|^2\right) - \frac{1}{\mu_0}\vec{\nabla} \cdot (\vec{E} \times \vec{B}) \tag{2.35}$$

$$\vec{S} \equiv \frac{1}{\mu_0}(\vec{E} \times \vec{B}) \tag{2.36}$$

$$\frac{\partial u}{\partial t} = -\vec{\nabla} \cdot \vec{S} \tag{2.37}$$

Where W is the total energy of the electromagnetic fields, $\vec{S}$ is denominated as Poynting vector and u is the energy per unit of volume, Griffiths (2017, p.358) says

about the Poynting's theorem: "The work done on the charges by the electromagnetic force is equal to the decrease in energy remaining in the fields, less the energy that flowed out through the surface", in other words, the Poynting vector represents the power (energy per unit of time) per unit of area transported by the fields. By this way, the power is minus the closed integral of the Poynting vector dot product with the area element that closes the fields.

2.1.4 Shielding Effect

When interacting with an object, the wave can be absorbed, reflected, suffer from multiple internal reflections or be transmitted, as seen in Figure 01. The absorbed power is the quantity of energy per unit time that gets internalized by the medium and can contribute to elevate the temperature, access higher energetical states and sometimes even change the thermodynamic properties of the media. Meanwhile the reflected power is the power that after a contact with the medium, inverts its propagation vector (gets mirrored). Mirrors and metallic foils are great reflectors because of their small skin depth, which prevents the wave from propagating through the media. Multiple internal reflection power is the power that is reflected by the inner walls of the medium. This kind of reflection depends on the wavelength of the incident (or former internal reflected wave, in the case of a second or multiple internal reflection) and on the thickness of the medium, usually, on microwave scales this phenomenon is very small and can be neglected. Finally, the transmitted power is the power that passes through the media reaching the other side.

Carvalho, A. *et al*. (2024) denote, on equations 2.38-2.41, by A, the fraction of absorbed power (or absorption coefficient). R the fraction of reflected power (or reflection coefficient). M the fraction of the power that gets multiple internal reflections (or multiple internal reflection coefficient), and T the fraction of the power that gets transmitted (or transmission coefficient). Due to energy conservation their summation becomes the unit (equation 2.42), which means that all the power (or energy) of the incident waves can be or absorbed, reflected, suffer from multiple internal reflections or be transmitted. Usually M is small compared with the others fractions due the dimensions of the samples and the incident frequency of microwave systems (and

their respectives wavelength), once that the larger the frequency, smaller the wavelength. So by definition and energy conservation:

$$A \equiv \frac{P_{abs}}{P_{inc}} \tag{2.38}$$

$$R \equiv \frac{P_{ref}}{P_{inc}} \tag{2.39}$$

$$M \equiv \frac{P_{mir}}{P_{inc}} \tag{2.40}$$

$$T \equiv \frac{P_{trans}}{P_{inc}} \tag{2.41}$$

$$A + R + M + T = 1 \tag{2.42}$$

Where P_{inc} stands for the incident power, P_{abs} stands for the absorbed power, P_{ref} stands for the reflected power, P_{mir} stands for the power contained due the multiple internal reflections and P_{trans} stands for the transmitted power. It is notable that for each medium, the respective power will be proportional to the square moduli of the electric (and magnetic) fields of the medium, and their respective proportions with respect to the incident square moduli of the electric (and magnetic) fields.

The shielding effect consists of blocking as much as one can, the passage of the incident waves through the medium. Nan *et al.* (2023) say that the attenuation of the transmission coefficient is the core of this process, the smaller the transmission coefficient, the better shielding a material presents. The mechanism consists in improving the absorption and reflection coefficients, since their summation is limited by 1 according to equation 2.42.

Akram, S. *et al.* (2023) say that a high electrical and thermal conductivity plays an important role on the shielding process, they enlarge the reflection and absorption coefficients, while magnetized materials, particularly those with high magnetic permeability, can exhibit shielding properties against certain types of electromagnetic interference. This is because they can redirect or absorb the magnetic component of the electromagnetic waves, improving both absorption and reflection coefficients. Multiple layered materials tend to have a significant contribution for the multiple internal reflection coefficient, since the difference on the permittivity and permeability

(on magnetic material) on the different media on the layers might contribute for this phenomenon.

Figure 1 - The mechanism behind the shielding effect.
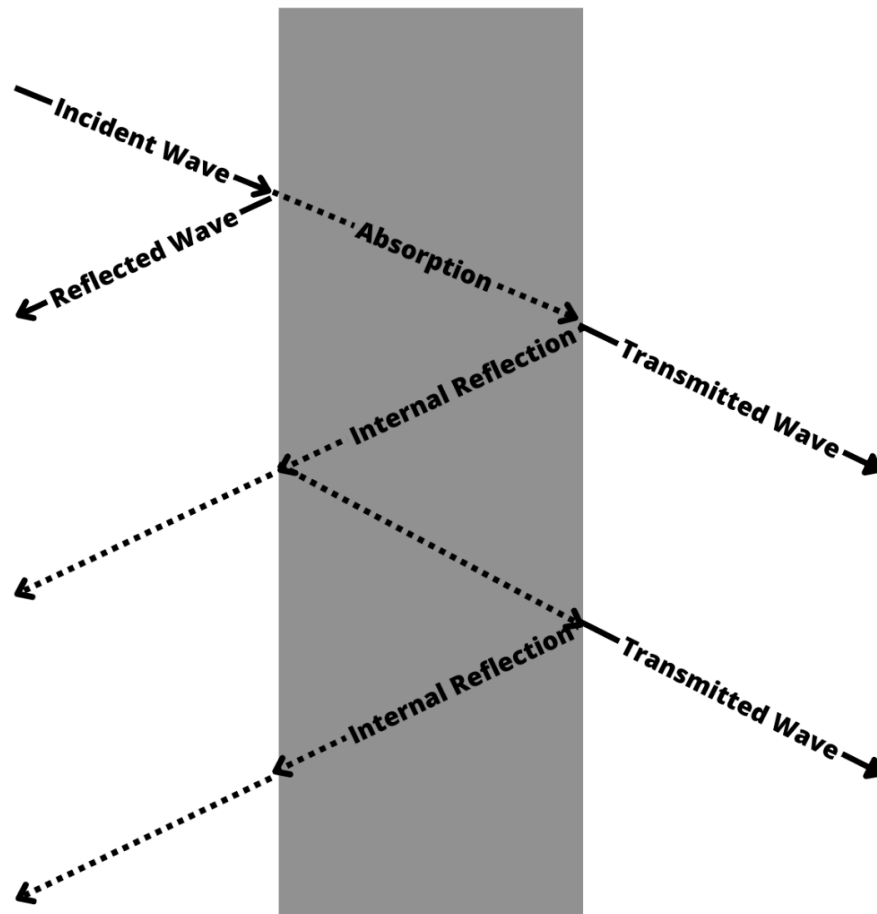
Source: The author.

2.2 MICROWAVE SPECTRUM

Microwave technology corresponds to the part of technological devices that operate with frequencies from orders of 10^9 Hz to 10^{11} Hz. On these systems there is a strong dependency with the frequency of several physical properties, such as permittivity and permeability, conduction, impedance, skin depth and many others. The applications of those kinds of devices are commonly found in computers, transmission lines, data transmission, and ferromagnetic resonance.

2.2.1 Microwave Bands

Light spectrum is wide. As seen approximately on Table 01, it varies over several orders of frequency and wavelength, from Radio Frequency (RF) to gamma rays, the difference of the frequency goes over the order of the nineteenth power of ten. Visible light, as microwave light, concerns only a small fraction of the total spectrum.

Table 1 - Light spectrum.

(Continue)

Classification	Wavelength (m)	Frequency (Hz)
Gamma Ray	10^{-14}	3×10^{21}
Gamma Ray	10^{-13}	3×10^{20}
Gamma Ray	10^{-12}	3×10^{19}
X-ray	10^{-11}	3×10^{18}
X-ray	10^{-10}	3×10^{17}
Far Ultraviolet	10^{-9}	3×10^{16}
Ultraviolet	10^{-8}	3×10^{15}
Visible	10^{-7}	3×10^{14}
Infrared	10^{-6}	3×10^{13}
Far Infrared	10^{-5}	3×10^{12}
Far Infrared	10^{-4}	3×10^{11}
Microwave	10^{-3}	3×10^{10}
Microwave	10^{-2}	3×10^{9}
Microwave	10^{-1}	3×10^{8}
Microwave	1	3×10^{7}

Table 01: Light spectrum.
(Conclusion)

Classification	Wavelength (m)	Frequency (Hz)
Radio Frequency	10	3×10^{6}
Radio Frequency	10^{2}	3×10^{5}
Radio Frequency	10^{3}	3×10^{4}
Long wave radio	10^{4}	3×10^{3}

Source: Self elaboration Griffiths (2017, p.396) and Pozar (2012, p.1).

According to Pozar (2012, p. 2) and Khan (2014, p. 4), microwave frequencies are divided into Bands as seen on Table 02, ranges of frequencies used for commercial and practical purposes. The most common band is the X band, it is used in Radar Systems, Satellite Communications and Scientific Research. The X band is chosen for these applications because it strikes a balance between having sufficiently short wavelengths for high-resolution applications and long enough wavelengths to penetrate certain materials and atmospheric conditions.

Khan (2014, p. 9-14) and Ulaby (2014, p. 7) say that L band is used in mobile communications such as 3G systems and old 4G generations, it is used in aviation for communication and navigation systems, GPS (Global positioning system), as satellite communication also works on the L band. S band is used for satellite communication and deep space research, military radars and communication (5G for exemple). C band is used for communication, radar and research. As said early, the X band is the most commonly used band for scientific research, thus in this work, all the research in EMI SE must be used on the X band. The bands above X band are usually used for radar, scientific and military applications.

Table 2 - Microwave bands and their frequency range.

Microwave Band.	Approximate Frequency (GHz).
L band	1–2
S band	2–4
C band	4–8
X band	8–12
Ku band	12–18
K band	18–26
Ka band	26–40
U band	40–60
V band	50–75
E band	60–90
W band	75–110
F band	90–140

Source: Pozar (2012, p. 2) and Khan (2014, p. 4).

2.2.2 Complex Permittivity (ϵ) and Permeability (μ) in the media

On microwave systems, the dependence of physical parameters with frequency is not uncommon; the higher the energy of a transmitted wave, and its frequency, the higher the likelihood of the appearance of nonlinear phenomena. Thus phenomena can directly interfere with how the energy is transferred or dispersed in the media. Thus it is necessary to assume not only a dependency with the frequency of the permittivity and permeability, but also, assume that both can now be complex numbers. In this section we shall see how the imaginary part of the mentioned physical properties are intrinsically correlated with the energy dispersion and loss of a media.

Ulaby (2014, p. 37) cite that in a medium with current density $\vec{J}$ and conductivity σ, the Ohm's law, given by equation 2.43, led to a complex relative

permittivity ($\epsilon_r = \epsilon/\epsilon_0$. Where ϵ is the permittivity in the medium and ϵ_0 is the permittivity on the free space) in the medium with formulas described in equations 2.44 and 2.45.

$$\vec{J} = \sigma \vec{E} \tag{2.43}$$

$$\epsilon_r = \epsilon' + i\,\frac{\sigma}{\omega\epsilon_0} = \epsilon' + i\,\epsilon'' \tag{2.44}$$

$$\epsilon'' = \frac{\sigma}{\omega\epsilon_0} \tag{2.45}$$

Where ω is the angular frequency (f/2π, where f is the frequency, where in this work is among the MW spectrum) and ϵ' and ϵ'' are respectively the real and the imaginary part of the permittivity, while i is the complex unit.

Pozar (2012, p. 20) and Ulaby (2014, p.49) describe that a medium is lossless, it means that it does not dissipate energy as thermal energy, if $\sigma = \epsilon'' = 0$. meanwhile it is a low-loss medium if $\epsilon''/\epsilon' \ll 1$, a lossy media if $\epsilon' \simeq \epsilon''$, a good conductor if $\epsilon'' \gg \epsilon'$ and a perfect conductor if $\epsilon'' = \infty$.

Meanwhile a non magnetic system presents $\mu = 1$, from equation 2.16 and 2.46 can be seen that it does not present intrinsic magnetization ($\vec{M}$), because in this case $\vec{B} = \vec{H}$, and $\vec{M} = 0$. Often on magnetic material, the relative permeability ($\mu_r = \mu/\mu_0$) is a complex number that characterizes the magnetic loss tangent ($tan(\delta_m)$), as can be seen in equations 2.47 and 2.48 and represents important information about how much energy is dissipated due magnetization. μ' and μ'' represent the real and complex parts of the permeability respectively, while i is the complex unit.

$$\vec{B} = \mu_0(\vec{M} + \vec{H}) \tag{2.46}$$

$$\mu_r = \mu' + i\,\mu'' \tag{2.47}$$

$$tan(\delta_m) = \frac{\mu''}{\mu'} \tag{2.48}$$

2.3 WAVEGUIDE THEORY

Waveguide theory lays the groundwork for comprehending how electromagnetic waves propagate within confined structures. Understanding the process involved in guiding a wave and the modes of propagation associated within a waveguide is crucial for optimizing its performance.

Colin (2012) describes a waveguide as a physical structure or device that is designed to confine and guide electromagnetic waves, typically in the microwave and optical frequency ranges. Waveguides play a crucial role in the transmission of electromagnetic signals in various applications, including telecommunications, radar systems, microwave engineering, and optical communications.

Waveguides are designed to confine and guide electromagnetic waves within a certain region, preventing the waves from spreading in free space. They come in various forms, each tailored to specific frequency ranges and applications, in this section there will be explored the rectangular and circular cases. Concerning the materials used for waveguides depend on the frequency range of operation and their application. Common materials include metal for microwave waveguides and dielectric materials for optical waveguides (SVELTO, 2010, p. 417 and MARCUVITZ, 1986, p.387). This work uses rectangular waveguides where the behavior is going to be studied in the next section.

2.3.1 Rectangular Waveguides

Electromagnetic waves within a waveguide can exist in different modes, each with a unique pattern of electric and magnetic fields. The modes are determined by the dimensions and geometry of the waveguide. Waveguides have a cutoff frequency, below which certain modes of electromagnetic waves cannot propagate. This property is used to control the frequency range of operation for specific applications.

The main main characteristic of a waveguide is to guide the waves in a preferential direction, often by making the electric or magnetic component of the other directions being led to zero. Jackson (1998, p. 359) defines the transverse magnetic (TM) waves when $B_z = 0$ (the magnetic field on the z direction is zero), and the boundary conditions are taken as $E_z|_S = 0$ (the electric field on the z direction over

the surface S is zero), where S is the surface of the waveguide. Meanwhile the transverse electric (TE) waves are described as when $E_z = 0$ everywhere, with boundary conditions of $\frac{\partial Bz}{\partial n}|_S = 0$. Where $\frac{\partial}{\partial n}$ is the normal derivative and S is the surface of the waveguide.

Collin (2012, p. 182-190) and Jackson (1998, p. 361-362) describe the equations for the TE and TM modes of a waveguide with dimensions of a and b, with a > b, as given on equations 2.49 to 2.54, with boundary conditions given in the last paragraph. For TE (TM) modes, E_z (B_z) is zero. And by this way, for the TE mode, one has a differential partial equation as depicted on equation 2.49. By separation of variables, B_z can be separated as the product $B_z = f(x)g(y)$, what after division by B_z on both sides leads to equation 2.50. The only way for equation 2.50 be zero is if that first term must be equal to a constant (let it be named by $-k_x^2$), while the second term of the summation must be equal to another constant (let us name it by $-k_x^2$). So by this means, with the countourn conditions given on the last page, k_x, k_y, k_c, and B_z are depicted as in equations 2.51-2.54.

$$\frac{\partial^2 B_z}{\partial x^2} + \frac{\partial^2 B_z}{\partial y^2} + k_c^2 B_z = 0 \tag{2.49}$$

$$\frac{1}{f}\frac{\partial^2 f}{\partial x^2} + \frac{1}{g}\frac{\partial^2 g}{\partial y^2} + k_c^2 = 0 \tag{2.50}$$

$$k_x = \frac{n\pi}{a}. \; n = 0, 1, 2, \dots \tag{2.51}$$

$$k_y = \frac{m\pi}{b}. \; m = 0, 1, 2, \dots \tag{2.52}$$

$$k_c = [(\frac{n\pi}{a})^2 + (\frac{m\pi}{b})^2]^{(1/2)} \tag{2.53}$$

$$B_z = A_{nm} cos(\frac{n\pi x}{a}) cos(\frac{m\pi y}{b}) \tag{2.54}$$

Similar equations occur on the TM modes. A typical waveguide has dimensions of $a = 2b$. The most common mode used for measurements is the dominant mode TE_{10}. On this mode $k_c = \frac{\pi}{a}$, and the frequencies remain between the speed of light divided by a and the speed of light divided by $2a$, as seen on equation

2.55. This phenomena creates the microwaves bands that are widely used to experiment over MW systems.

$$\frac{c}{2a} < f < \frac{c}{a} \tag{2.55}$$

2.3.2 Waveguide Dimensions for Microwave Bands

Each dimension on a rectangular waveguide is defined by Table 03 for the following frequencies. These dimensions certify that only one mode will dominate over the range of frequencies on the determined microwave band and will be used on section 2.5 for the experimental procedure.

Table 3 - Waveguide dimensions and models that can be used over MW systems.

Microwave Band	Waveguide Name	Waveguide Dimensions (mm)
L band	WR-650	165.10 × 82.55
S band	WR-284	72.14 × 34.04
C band	WR-187	34.85 × 15.80
X band	WR-90	22.86 × 10.16
Ku band	WR-62	15.80 × 7.90
K band	WR-42	12.95 × 6.48
Ka band	WR-28	7.11 × 3.56
U band	WR-19	4.77 × 2.39
V band	WR-15	3.76 × 1.88
E band	WR-12	3.10 × 1.55
W band	WR-10	2.54 × 1.27
F band	WR-8	2.03 × 1.02

Source: Mathur and Raman (2020) and Khan (2014, p.4).

2.4 VECTOR NETWORK ANALYZER

As networks have grown in complexity and diversity, so too have the tools used to monitor and analyze them. In the dynamic landscape of modern networking, the demand for robust tools to monitor, analyze, and optimize network performance has given rise to innovative solutions, among which Vector Network Analyzers (VNAs) stand out as pivotal instruments. VNAs differentiate themselves through a rich set of features that extend beyond conventional network analyzers. This part of the section details the key functionalities of VNAs.

2.4.1 S-Parameters

Collin (2001, p.248-249) and Marcuvitz (1986, p. 106-107) describe that in microwave networks, the tangential electric (E_T) and magnetic (B_T) field can be calculated as functions of the vector mode functions characteristic of the transverse form of the dominant mode (e_m and h_m), and by the complex amplitudes of the electric field in the incident and reflected wave components of the dominant mode field, a_m and b_m respectively), as seen in equations 2.56 and 2.57.

$$E_T(x, y) = (a_m + b_m)e_m \tag{2.56}$$

$$B_T(x, y) = (a_m - b_m)h_m \tag{2.57}$$

> [...] The fundamental existence theorem applicable to the scattering formulation of a field problem states that the amplitudes of the scattered waves at the various terminals are uniquely related to the amplitudes of the incident waves thereon. Therefore, by superposition the amplitudes of the scattered waves arising from the simultaneous incidence of waves of amplitudes $a_1, \dots , a_N$. (MARCUVITZ, 1986, p.107).

This form a system of equations for b_N as given on equations 2.58-2.60, which led to the scattering matrix described on equation 2.61.

$$b_1 = S_{11}a_1 + S_{12}a_2 + \ldots + S_{1N}a_N \tag{2.58}$$

$$b_2 = S_{21}a_1 + S_{22}a_2 + \ldots + S_{2N}a_N \tag{2.59}$$

$$\vdots$$

$$b_N = S_{N1}a_1 + S_{N2}a_2 + \ldots + S_{NN}a_N \tag{2.60}$$

$$S = \begin{pmatrix} S_{11} & S_{12} & \ldots & S_{1N} \\ S_{21} & S_{22} & \ldots & S_{2N} \\ . & . & \ldots & . \\ . & . & \ldots & . \\ . & . & \ldots & . \\ S_{N1} & S_{N2} & \ldots & S_{NN} \end{pmatrix}$$

$$\tag{2.61}$$

The S matrix is known as the scattering matrix and represents scattering parameters (S-Parameters) from a N ports vector network analyzer. In this work, a two ports network analyzer will be used, as described in section 2.5.

2.5 EXPERIMENTAL SETUP

For this experimental set, the range of frequencies is generated over a two-port VNA, model E5063A, as seen in Figure 02, which gives the following Scattering parameters (S-parameters), usually complex values. The reflection coefficients are given by S_{11}, the input reflection coefficient, and S_{22}, the reverse reflection coefficient, while the transmission coefficients are given by S_{21}, the forward transmission coefficient, and S_{12}, the reverse transmission coefficient. Figure 03 Shows how the S-parameters are obtained from the two ports VNA.

The core of the experimental arrangement comprises two rectangular waveguides meticulously crafted for the X-Band frequency range. These waveguides function as the conduits for transmitting and receiving electromagnetic signals.

Wang, H. *et al.* (2021) cite that an anechoic chamber, purpose-built for EMI measurement, establishes a controlled environment, significantly mitigating external electromagnetic interference to ensure the precision of testing. The VNA acts as a

signal generator, emitting electromagnetic waves within the X-Band frequency range, which then function as the incident electromagnetic waves for the testing procedure.

Figure 2 - Two-port VNA, model E5063A used for measurements.

Source: The author.

Liu, X. *et al.* (2014) say that directional couplers facilitate the simultaneous measurement of both incident and transmitted electromagnetic waves, a key factor for accurate S-parameter measurements. To seamlessly connect the waveguides to the VNA and other testing equipment, waveguide transitions are employed, ensuring a smooth flow of electromagnetic signals. A specialized sample holder or fixture securely positions the iron nanowire sample within the waveguides, ensuring precise alignment and consistent results.

A computer, equipped with specialized measurement software, takes charge of controlling the VNA, recording measurement data, and conducting in-depth data analysis. Calibration standards, including short, open, and load standards, are implemented to calibrate the VNA, rectifying any system imperfections and guaranteeing measurement accuracy. Notwithstanding these calibrations, measurements are conducted both with and without the samples to calibrate the system itself.

Figure 3 - How the S-parameters are acquired by a two-port VNA.
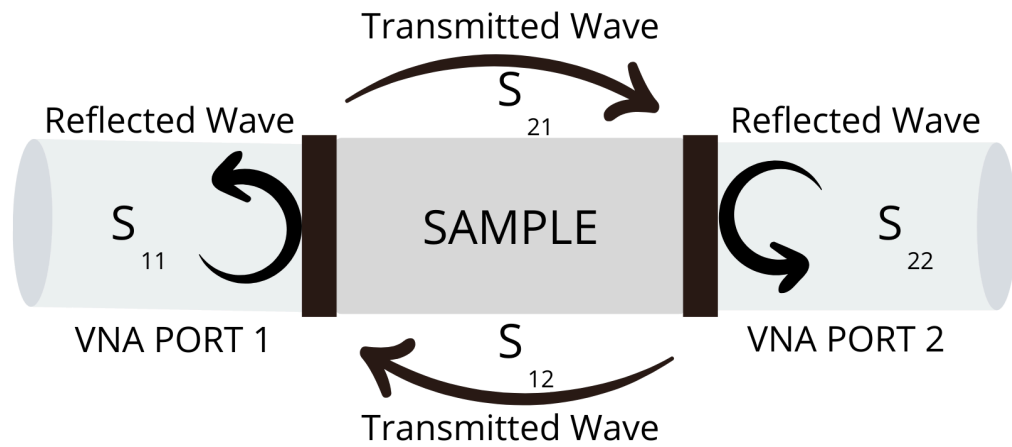
Source: The author.

Figure 4 - Sketch of the experimental setup.
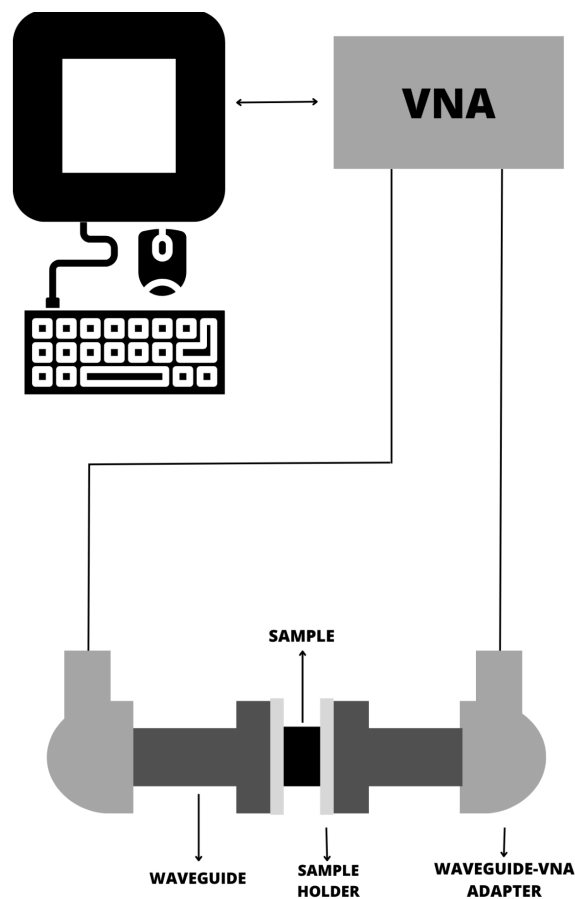
Source: The author.

Figure 04 shows the sketch of the experimental setup, the computer connected to the VNA, while both ports of the VNA are connected with the

waveguide coupler adaptors and the waveguides are mechanically connected to the chamber where the sample is held. The chamber with two transparent films of commercial acetate and covered, encapsulated and bonded in multiple layers of ethylene vinyl acetate (EVA), which prevents the sample from mechanical impacts, shocks, slides and any other possible mechanical interference on the sample position while the measurements.

2.6 ELECTROMAGNETIC INTERFERENCE SHIELDING EFFECTIVENESS

As our reliance on electronic devices continues to grow, the susceptibility to electromagnetic interference (EMI) becomes a critical concern in various industries. The ability to mitigate and control EMI is paramount, and the effectiveness of shielding materials is a key factor in achieving this goal. This section explores the concept of Electromagnetic Interference Shielding Effectiveness (SE) and its significance in safeguarding electronic systems. By investigating the fundamental principles, measurement methodologies, and real-world applications of shielding effectiveness, this section aims to provide a comprehensive understanding of the strategies employed to combat electromagnetic interference.

Wanasinghe, Aslani and Ma (2020) say that Electromagnetic Interference Shielding Effectiveness is a quantitative measure of a material's ability to attenuate electromagnetic signals. The accurate assessment of shielding effectiveness involves standardized measurement techniques described in section 2.1.4, the practical calculation for EMI SE shall be described in the following sections such as the qualification of the shielding and its potential control parameter. The practical applications of electromagnetic interference shielding are widespread, ranging from consumer electronics to military and medical devices, thus commercial and security standards must be assigned.

2.6.1 EMI SE from Physical Quantities

Merizgui *et al.* (2021) indicate that the EMI SE can be measured due the comparison of the transmitted and incident power, electric field, or magnetic field (denoted by P_{trans}, P_{inc}, E_{trans}, E_{inc}, H_{trans} and H_{inc}). By the following equations 2.62-2.64.

$$SE_T = 10 \, log_{10}(P_{trans} / P_{inc}) \tag{2.62}$$

$$SE_T = 20 \, log_{10}(E_{trans} / E_{inc}) \tag{2.63}$$

$$SE_T = 20 \, log_{10}(H_{trans} / H_{inc}) \tag{2.64}$$

2.6.2 EMI SE from S-Parameters

Ji *et al.* (2018) argue that the symmetric arrangement of the scheme on Figure 03, leads to the match of the moduli of reflection and transmission, bringing the equations 2.65-2.66:

$$|S_{11}| = |S_{22}| \tag{2.65}$$

$$|S_{21}| = |S_{12}| \tag{2.66}$$

As mentioned in section 2.1.4, due to energy conservation, it is straightforward that the energy lost in the process of reflection, absorption and multiple internal reflections added to the energy of the transmitted waves sums up as the total energy of the incident wave as seen in equation 2.42. In terms of the S-parameters, those coefficients are given for the equations 2.67-2.69:

$$A = 1 - |S_{11}|^2 - |S_{21}|^2 \tag{2.67}$$

$$R = |S_{11}|^2 = |S_{22}|^2 \tag{2.68}$$

$$T = |S_{12}|^2 = |S_{21}|^2 \tag{2.69}$$

Zhang *et al*. (2019) imply that the total EMI SE (SE_T) can be divided into the respective summation of the reflected, absorbed and multiple internal reflection, respectively denominated as SE_R, SE_A and SE_M. For which SE_M becomes insignificant for values of SE_T above 10 dB -15 dB (WANG, Y. *et al*., 2020). Where in terms of the wave coefficients and S-Parameters the equations 2.70-2.73 are given as:

$$SE_T = SE_R + SE_A + SE_M \tag{2.70}$$

$$SE_R = -10\,log_{10}\,(1 - R) = -10\,log_{10}\,(1 - |S_{11}|^2) =$$
$$-10\,log_{10}\,(1 - |S_{22}|^2) \tag{2.71}$$

$$SE_A = 10\,log_{10}\,((1 - R)/T) = 10\,log_{10}\,((1 - |S_{11}|^2/|S_{21}|^2) \tag{2.72}$$

$$SE_T = -10\,log_{10}\,(T) = -10\,log_{10}\,(|S_{12}|^2) = -10\,log_{10}\,(|S_{21}|^2) \tag{2.73}$$

In this experiment, the adjustment on the total EMI SE was made after the calibration from the calibration kit for the VNA and by subtracting the values for the set without sample from the set with sample. The standards followed for EMI SE were described by IEEE (2007).

3 PREPARATION OF THE NANO AND CARBON-BASED COMPOUNDS

3.1 YTTRIUM IRON GARNET (YIG)

Yttrium Iron Garnet (YIG) is a synthetic crystalline material that belongs to the garnet family. Its chemical formula is $Y_3Fe_5O_{12}$. Luo, H. *et al.* (2024) say that YIG is known for its cubic structure, ferromagnetic, low loss and temperature stability properties, making it a valuable material in various applications, particularly in the field of microwave technology. The YIG shielding will be measured in section 4.1.

3.1.1 Preparation of the YIG

The preparation of nano elongated structures of Yttrium iron garnet ($Y_3Fe_5O_{12}$, YIG) deposed on a thin porous membrane of alumina was made using a sol-gel methodology described by Hayati *et al*. (2018), within the starting materials of Iron (III), nitrate ($Fe(NO_3)_3.9H_2O$), Yttrium nitrate ($Y(NO_3)_3.6H_2O$) and citric acid ($C_6H_8O_7.H_2O$). The method begins with the desolvation of the nitrates in deionized water, later, a sol precursor was prepared by mixing a 3:5 stoichiometric of Y and Fe. The mixture was stirred for 1h at room temperature, and then the citric acid was added with a stoichiometric ratio of 1:1 with the nitrate.

Figure 5 - Alumina membrane.

Source: The author.

Pessoa *et al.* (2023) used a vacuum system at 0.001 Torr coupled to a syringe body and a steel mesh as a carrier on top of the syringe, a porous aluminum oxide membrane (alumina), as seen on Figure 05, (disc diameter of 47 mm and pore diameter of 200 nm, Sigma Aldrich), and the sample was then heated in an electric oven, undergoing a heat treatment consisting of two steps: a heating one, with rate of 10°C or 1ºC per minute to reach 900 °C, remaining at this temperature for 2h, at which the YIG phase was formed, then cooled with the same rate until the samples obtain room temperature.

3.1.2 Characterization of the YIG

Figure 6 - YIG X-Ray diffraction.
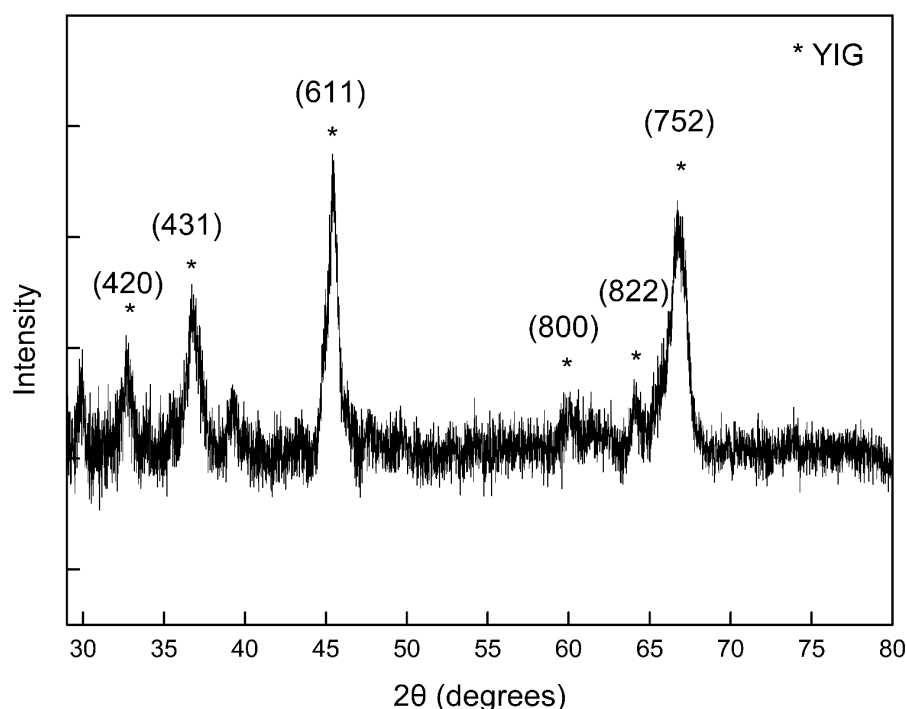
Source: Pessoa *et al* (2023).

To assess the chemical composition of the composite material situated within the nanopores of the template, Pessoa *et al.* (2023) utilized X-ray diffraction (XRD) through a Rigaku SmartLab model equipped with Cu-Kα radiation (wavelength of 1.541874 Å). The acquired data underwent analysis employing the synthesis process for elongated nanostructures within the alumina porous membrane as seen in Figure 06. For visualizing the deposition within the pores, a gold layer of about 10 nm thickness was applied to metallize the template, and scanning electron microscopy

(SEM) was conducted using a Zeiss Auriga model as seen on Figure 07, the nano elongated structure of YIG are uniform but with small deformations.

Figure 7 - Scanning electron microscopy of YIG. a)Inclined view. b)Horizontal view.
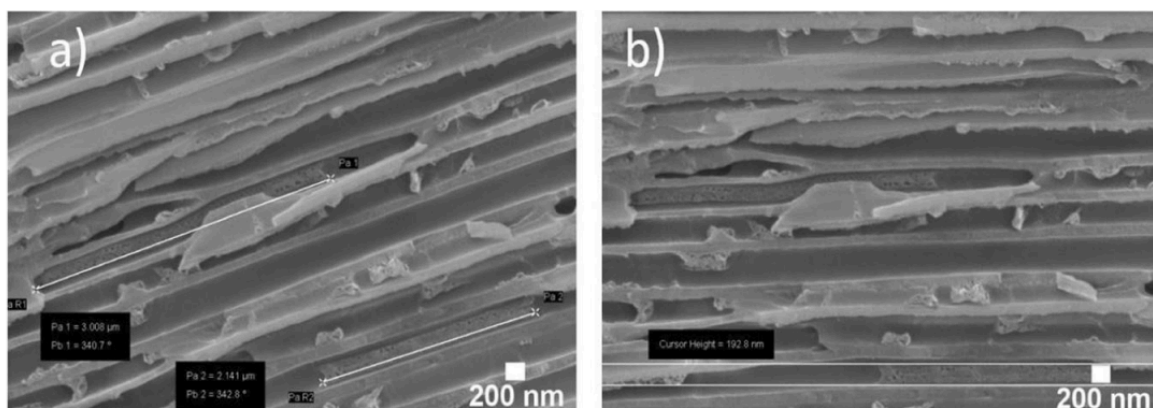
Source: Pessoa et al. (2023).

3.2 BACTERIAL CELLULOSE

Bacterial cellulose (BC) is a form of cellulose (a complex carbohydrate that serves as the main structural component in the cell walls of plants or bacteria) and can be acquired from different microorganisms. For this work, the microorganism utilized for the production of the BC films was the bacteria Gluconacetobacter Hansenii UCP1619, acquired from the *Banco de Culturas do Núcleo de Pesquisas e Ciências ambientais e Biotecnologia* (NPCIAMB) of the *Universidade Católica de Pernambuco* (UNICAP). The samples can be seen in Figure 08. The shield of BC compounds will be measured in section 4.2.

3.2.1 Preparation of Bacterial Cellulose

The microorganism was cultivated in HS medium, as described by Hestrin and Schramm (1954) and modified by Hungund and Gupta (2010). This medium consists of 2.0% glucose (m/v), 0.5% yeast extract (m/v), 0.5% peptone, 0.27% Na_2HPO_4 (m/v), and 0.15% citric acid (m/v).

The pre-inoculum, a small culture that is grown before the main inoculation or cultivation process (It serves as an initial population of actively growing cells that can be introduced into a larger culture or medium to initiate and accelerate the growth of

the desired microorganisms.), was prepared following the method outlined by Costa *et al.* (2017) and Galdino *et al.* (2019). Initially, the bacteria were activated by inoculating them on HS agar medium and incubating at 30 °C for 48 hours. The active cells were then used to prepare the pre-inoculum, which was carried out in liquid HS medium for 48 hours at 30 °C.

The medium used for the BC fermentation was as described by Costa *et al*. (2017) and Galdino *et al.* (2019), containing 1.5% glucose, 2.5% corn steep liquor, 0.27% Na_2HPO_4, 0.15% citric acid, pH 5, with the addition of 3% of the obtained pre-inoculum. The production of the BC membranes was carried out statically at 30°C for 10 days of growth. After production, the BCs were cleaned and purified by immersion in boiling water for 2 hours, then exposed to UV light for 1 hour, and finally rinsed with deionized water.

On the compounds with magnetite, the coprecipitation of magnetite, in all the conducted processes, followed a model similar to that described by Chanthiwong *et al.* (2020) and Salles *et al.* (2022), with adaptations. In their work, the authors reproduced the following chemical equations:

$$Fe^{2+} + 2Fe^{3+} + 8OH^- \rightarrow Fe_3O_4 + 4H_2O$$
$$2FeCl_3 + FeCl_2 + 8NH_3 + 4H_2O \rightarrow Fe_3O_4 + 8NH_4Cl$$
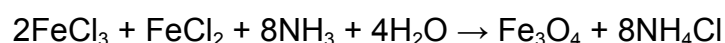
The incorporation methodologies were performed using both whole and processed cellulose films. For the processing, an Oster mixer, model FPSTHB2610R 017, was employed.

To save time, the simultaneous precipitation of more than one compound at time was searched, this process is called coprecipitation, and it occurred in two different ways. The *in situ,* where the BC films were immersed in a solution of iron (II and III) chloride in a molar ratio of 1:2, where they were left at rest. After 48 hours, the iron-impregnated BCs were placed in an aqueous solution containing 8 moles of 28% NH_4OH for 30 minutes, taking on a dark color, indicative of the formation of Fe_3O_4 within the films. Following coprecipitation, the produced materials were dried in two ways, using an oven and a lyophilizer. And *ex situ*, where to obtain magnetite crystals, a solution of iron (II and III) chloride in a molar ratio of 1:2, respectively, was prepared at room temperature. Slowly and gradually, an aqueous solution containing 8 moles of 28% NH_4OH was added to the chloride solution over 0.5 hours. The

reaction occurred as described in the previous chemical equations, resulting in an aqueous solution of magnetite. After this process, the magnetite nanoparticles settled, and the supernatant was removed. The particles were then resuspended in distilled water, where BC membranes were immersed for 48 hours. Finally, the formed materials were collected and dried using both an oven and a lyophilizer.

The oven drying was carried out in a device with air circulation at 60°C for 48 hours, resulting in the following samples: BC-COMAG-OVEN (whole BC with *in situ* coprecipitation of magnetite, dried in an oven), PBC-COMAG-OVEN (processed BC with *in situ* coprecipitation of magnetite, dried in an oven), BC-MAG-OVEN (whole BC with *ex situ* coprecipitation of magnetite, dried in an oven), PBC-MAG-OVEN (processed BC with *ex situ* coprecipitation of magnetite, dried in an oven).

For freeze-drying, the membranes were first frozen for 48 hours and then dried in a lyophilizer for an additional 48 hours. The obtained samples were named as follows: BC-COMAG-LYO (whole BC with *in situ* coprecipitation of magnetite, lyophilized), PBC-COMAG-LYO (processed BC with *in situ* coprecipitation of magnetite, lyophilized), BC-MAG-LYO (whole BC with *ex situ* coprecipitation of magnetite, lyophilized), PBC-MAG-LYO (processed BC with *ex situ* coprecipitation of magnetite, lyophilized).

Figure 8 - Materials obtained at the end of the magnetite incorporation processes into BC films.

BC-MAG-OVEN   BC-MAG-LYO   PBC-MAG-OVEN   PBC-MAG-LYO

BC-COMAG-OVEN BC-COMAG-LYO PBC-COMAG-OVEN PBC-COMAG-LYO
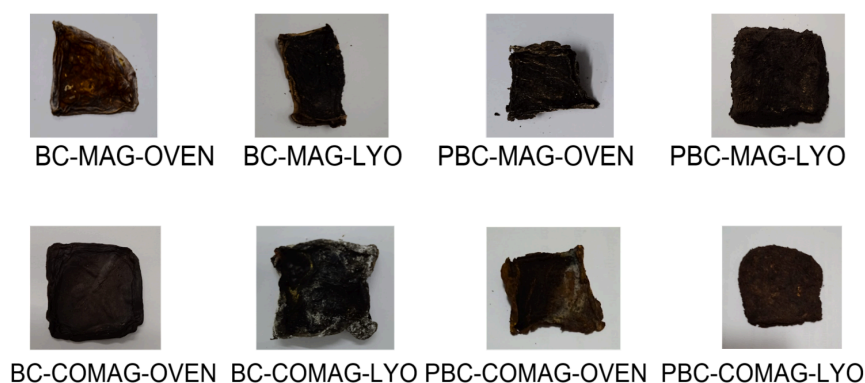
Source: The author.

3.3 Fe$_3$O$_4$@NITROGEN-DOPED REDUCED GRAPHENE OXIDE AEROGEL

Xu *et al.* (2023) and Olumurewa *et al.* (2023) say that graphene oxide is a modified form of graphene with oxygen-containing groups added to its surface, while reduced graphene oxide (rGO) is the product of the reduction of the oxygen-containing groups, what brings back certain properties of the graphene, like high conductivity. Chhetri *et al.* (2019) say that nitrogen-doped graphene oxide (NrGO) is the product of rGO doped with nitrogen, improving the conductivity of it, while the addition of the EMI SE. The shield of Fe$_3$O$_4$@NrGO will be measured in section 4.3.

3.3.1 Preparation of Fe$_3$O$_4$@NrGO aerogel

The preparation of Fe$_3$O$_4$@NrGO aerogel consisted of three steps, as described for Carvalho *et al.* (2024). The first step was the synthesis of the NrGO aerogel, the second step was the synthesis of the Fe$_3$O$_4$ nanoparticles (NP), the final step was the incorporation of the Fe$_3$O$_4$ NP at the NrGO aerogel.

The first step consisted in using the Hummers method, which involved the incorporation of urea into a suspension containing 1 mg/mL of graphene oxide (GO), utilizing a mass ratio of 300:1 (urea:GO), the introduction of urea to the GO suspension, and the resulting mixture underwent sonication in a specialized bath operating at 40 kHz and 55 W. To contrast and obtain the material without nitrogen doping (rGO), an analogous procedure was employed, omitting the addition of urea. The synthesis conditions were rigorously controlled, maintaining a temperature of 180°C for a duration of 12 hours.

The second step was the fabrication of the Fe$_3$O$_4$ NP, and it was conducted employing the co-precipitation technique, a widely recognized method for the preparation of magnetic nanoparticles. The procedure commenced with the addition of 30 mmol of ferric chloride and 15 mmol of ferrous chloride in a molar ratio of 2:1 to 400 mL of distilled water contained within a 1 L Erlenmeyer flask. Lately, a magnetic field was used to separate the particles.

The final step was the preparation of the Fe$_3$O$_4$@NrGO composite by ex-situ synthetic approach reported, immersing the NrGO aerogel in a Fe$_3$O$_4$ suspension with a proportion of 1 mg $\cdot$ mL^{-1} for 4 days.

3.3.2 Characterization of Fe$_3$O$_4$@NrGO aerogel

Carvalho *et al.* (2024) made the analysis of the structure of NrGO, what involved conducting XRD assessments on graphene compounds, as seen in Figure 09, The distinctive peaks on the main plane (002) at 25.1° and 24.8° signify rGO and NrGO. Both rGO and NrGO revealed 5 layers, with interplanar distances of 0.354 nm for rGO and 0.359 nm for NrGO. The identification of Plane (10) at 43.1° indicates structures with haphazard layer arrangements, pointing to a turbostratic nature in the synthesized rGO and NrGO.

Figure 9 - XRD of Fe$_3$O$_4$@NrGO.
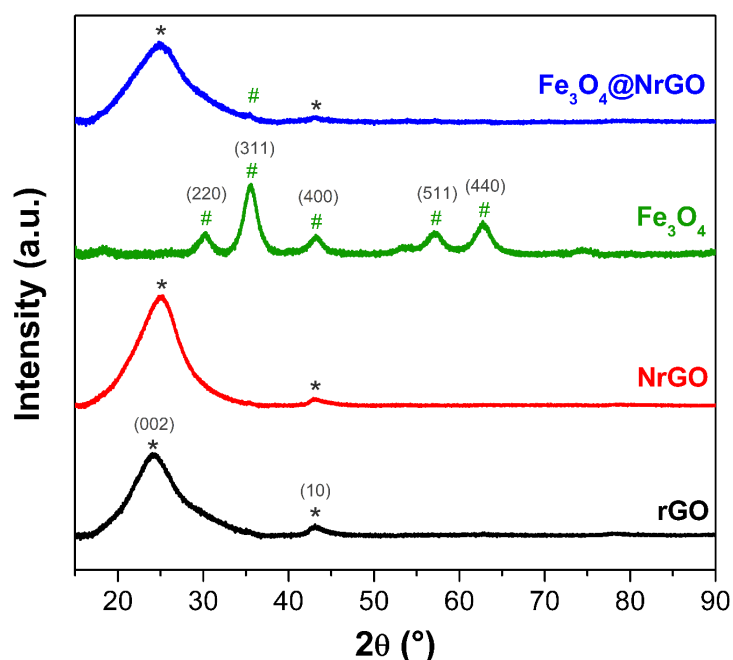
Source: Adapted from Carvalho *et al.* (2024).

Figure 10, adapted from Carvalho et al. (2024) shows the SEM of the Fe$_3$O$_4$@NrGO compounds, as described early, it is visible the turbostratic nature of the probe. Common characteristics of rGO were observed, like folded and grooved, ruffled layers.

Figure 10 - SEM of Fe$_3$O$_4$@NrGO.
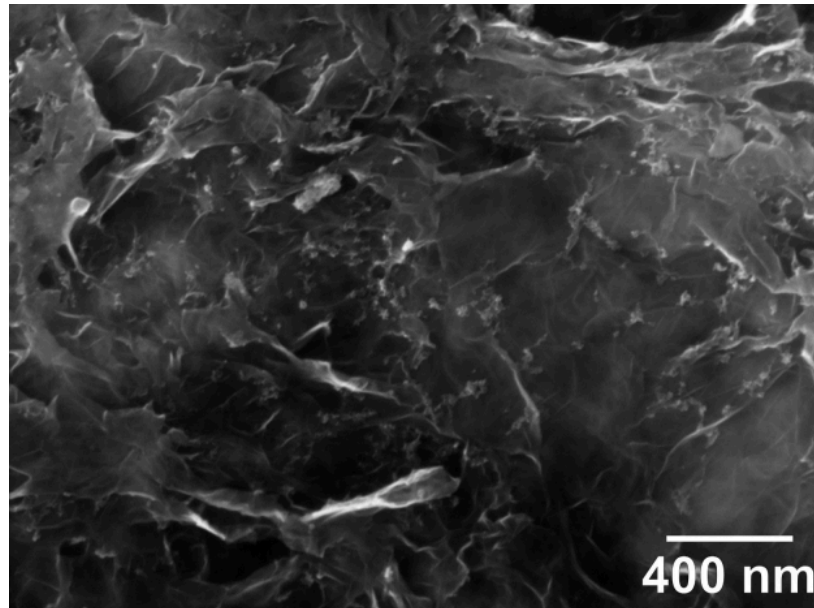
Source: Carvalho *et al.* (2024).

3.4 COBALT NANOWIRES

Ha *et al.* (2022) say that "Nanowires (NW) are structures with diameters in the nanometer scale and micrometer lengths with a high aspect ratio (AR), which classifies them as quasi-one-dimensional (1D) materials", while Hsu *et al.* (2023) say that metal nanowires "[...] promise great performance in electronic components thanks to their special properties. the event of electronics and gaining power during this field depends on continuous progress in shrinking electronic components". Apart from these properties, the study of the EMI SE on NW has been growing (WANG, G. *et al.*, 2022) which gives a glimpse for future applications. The shield of CoNW will be measured in section 4.4.

3.4.1 Preparation of the cobalt nanowires

This part of the project was based on Castro-Lopes *et al*. (2023) and França *et al.* (2023), nanowires were produced by the electrodeposition method. Porous alumina membranes were used to fabricate nanowires (13 mm in diameter - Whatman®) with pore diameters of approximately 200 nm. 50 nm of gold was

metallized at one side of the membrane with a BAL-TEC SCD 050 evaporator. In this study, we utilized three samples: the first sample, comprising a commercially available alumina porous membrane metallized with gold, designated as $Au^0@Al_2O_3$. In the second sample, we grew cobalt nanowires, named $Co^0+Au^0@Al_2O_3$. The third sample consisted of nickel and cobalt wires, denoted as $NiCo+Au^0@Al_2O_3$.

The electrolyte used for $Co^0+Au^0@Al_2O_3$ consisted of 0.5 M heptahydrate cobalt sulfate $[CoSO_4.7H_2O]$, 0.5 M boric acid $[H_3BO_3]$, and distilled water as the solvent with reduction potential of -1.20 V for 10 minutes. For the $NiCo+Au^0@Al_2O_3$ sample, the electrolyte remained the same, with the addition of 0.5 M hexahydrated nickel sulfate $[NiSO_4.6H_2O]$ with potential of -1.20 V for 8 minutes. We employed an Invium potentiostat, model INVIUMSTAT.XR, to control the electrodeposition parameters. Nanowire synthesis took place in a three-electrode electrolytic cell, with Ag/AgCl serving as the reference electrode, Pt as the counter electrode (anode), and Au as the working electrode (cathode). Chronoamperometry mode was applied for $Co^0+Au^0@Al_2O_3$ and $NiCo+Au^0@Al_2O_3$, where the potential was fixed, and the current varied over time.

3.4.2 Characterization of the cobalt nanowire

To present the characterization of the cobalt nanowires, a Rigaku Smartlab Cu-Kα X-ray diffractor was used, and as seen on Figure 11, the gold phase was found as seen in Figure 11a), while on the cobalt nanowires, a cobalt+gold phase was seen as in Figure 11b), and finally on Figure 11c), the NiCo+gold nanowires were detected.

For scanning electron microscopy the image of the gold membrane beholding with the nanowires, a Tescan MIRA3 scanner was used as mentioned in section 3.1.2. Figure 12a) shows the SEM of the cobalt nanowire, while Figure 12b) shows the SEM of the NiCo nanowires. Respectively, the thickness of the samples were 0.093 mm and 0.092 mm.

Figure 11 - XRD of Cobalt nanowires. a)$Au^0@Al_2O_3$. b)$Co^0+Au^0@Al_2O_3$. c)$NiCo+Au^0@Al_2O_3$.
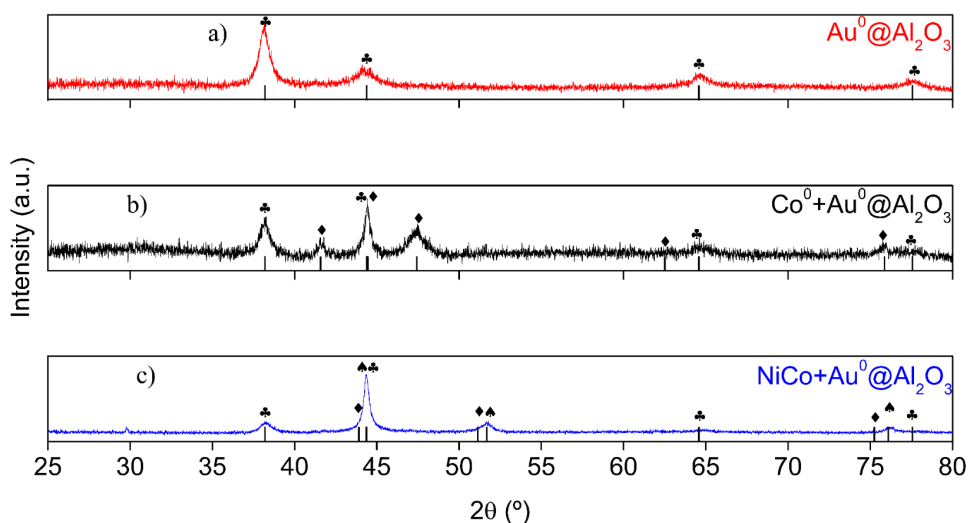
Source: adapted from Castro-Lopes *et al.* (2023).

Figure 12 - SEM of the cobalt nanowires. a)$Co^0+Au^0@Al_2O_3$. b)$NiCo+Au^0@Al_2O_3$.
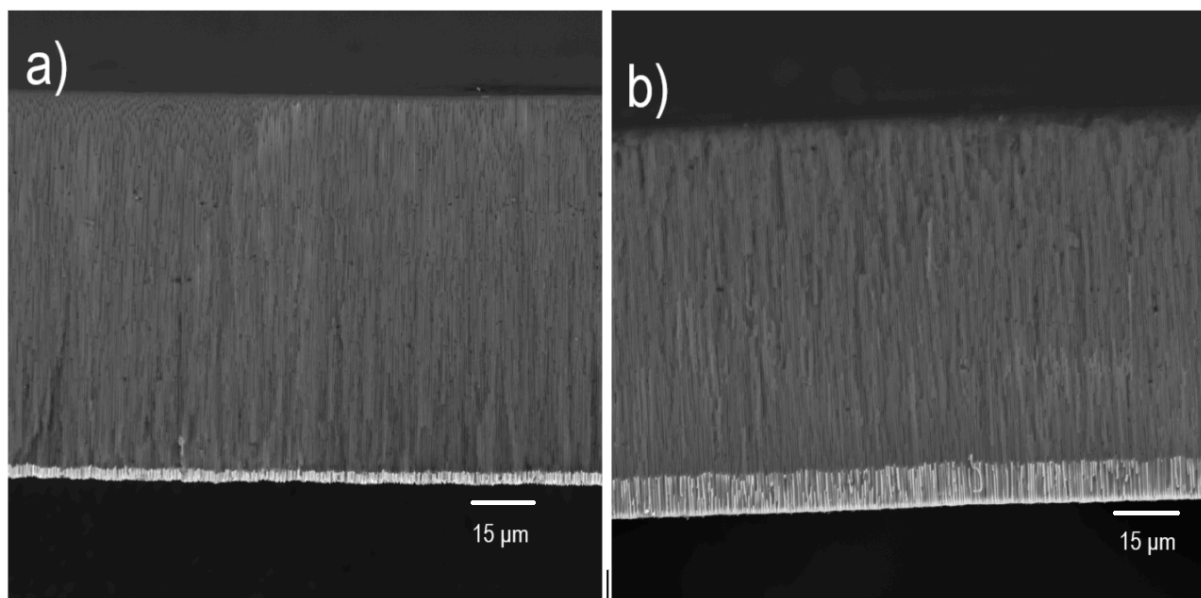
Source: Adapted from Castro-Lopes *et al.* (2023).

3.5 IRON NANOWIRES

The search for implements of iron nanowires, as a 1D structure, in diverse systems has grown in the last decade, mostly due to its relatively suitable conductivity and high aspect ratios (LI *et al.* 2023), photocatalytic applications

(LERICI *et al.* 2022) and its magnetic performance. Lipiec, Sobczak and Trzeciak (2015) say that "an object with an elongated shape made of ferromagnetic material, such as the ferromagnetic particles used, is characterized by a large magnetic moment in an external rotational magnetic field". In this work the shield of FeNW will be searched in section 4.5.

### 3.5.1 Preparation of iron nanowires

This part is similar with section 3.4.1, França *et al.* (2023) said that iron nanowires were obtained by electrodeposition through the utilization of commercial porous alumina membranes with a pore diameter of approximately 200 nm. Preceding the electrodeposition process, a thin layer of gold (Au) was sputtered on one side of the membrane to seal the pores and serve as the working electrode. The electrodeposition of iron wires was executed employing an Iviumstat.XR potentiostat, featuring a platinum counter electrode and an Ag/AgCl reference electrode. The membranes underwent immersion in an electrolytic solution comprising $C_6H_8O_6$ (0.005 M), $FeSO_4 \cdot 7H_2O$ (0.5 M), and H_3BO_3 (0.25 M) at a temperature of 25°C. The deposition process was sustained for 15 minutes under a -1.5 V potential.

3.5.2 Characterization of the iron nanowires

The characterization was performed as in section 3.4.2 and 3.1.2, leading to the performance of the X-ray diffraction by a Rigaku SmartLab model implementing Cu-Kα radiation (wavelength of 1.541874 Å) and supplied Figure 13, where can be seen the Iron phases, the gold phase on the thin membrane and also the formation of Fe_2O_3 and Fe_3O_4, commonly obtained in the process of oxidation of the iron nanowires.

Figure 14 provides the SEM imaging enabled a qualitative assessment of the interfaces between the iron nanowires and the gold template, elucidating any potential crystallographic orientations or defects. Such a detailed analysis is crucial for optimizing the synthesis process and tailoring the properties of these nanowires for specific applications, ranging from nanoelectronics to catalysis. As in the section 3.4.2, The SEM was made using a Tescan MIRA3 model and found 0.065 mm thickness for the iron nanowires.

Figure 13 - XRD of iron nanowires.
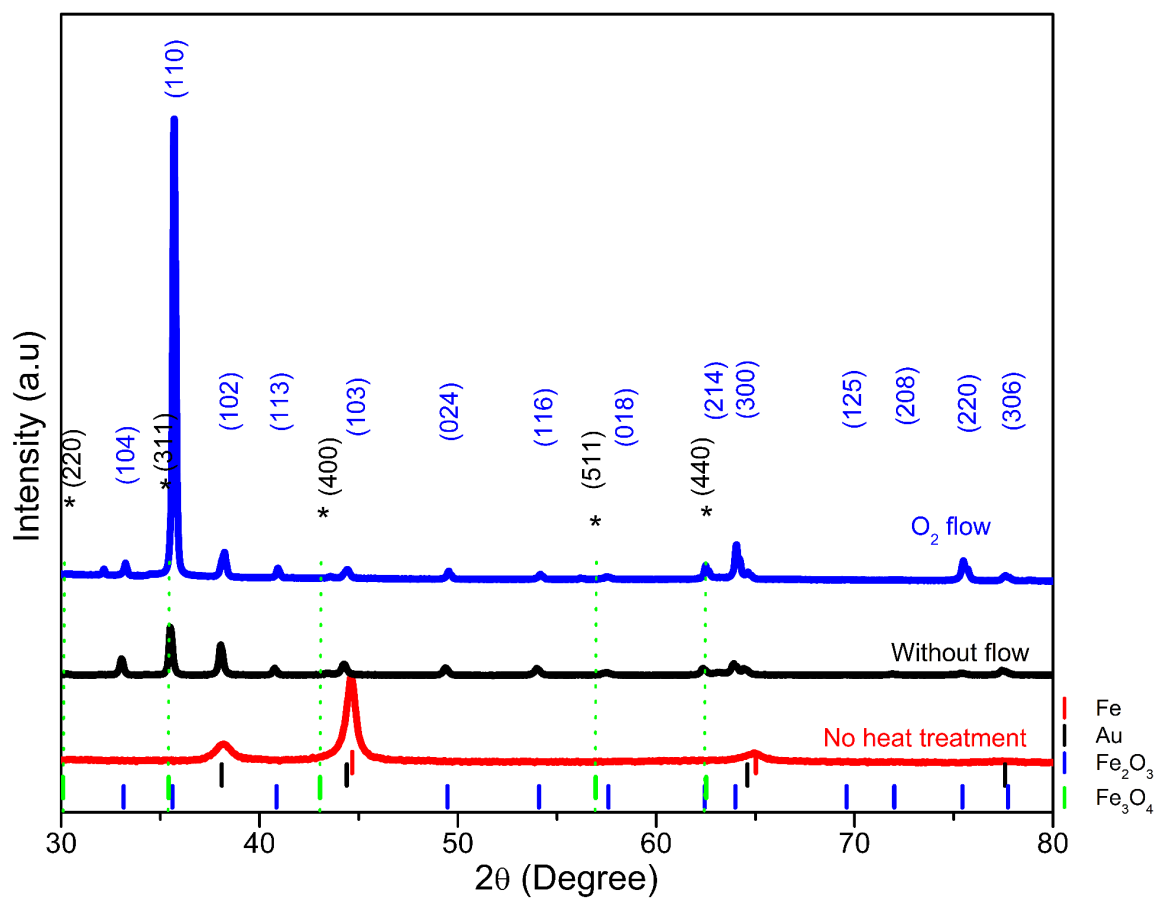
Source: França et al (2023).

Figure 14 - SEM of the iron nanowire.
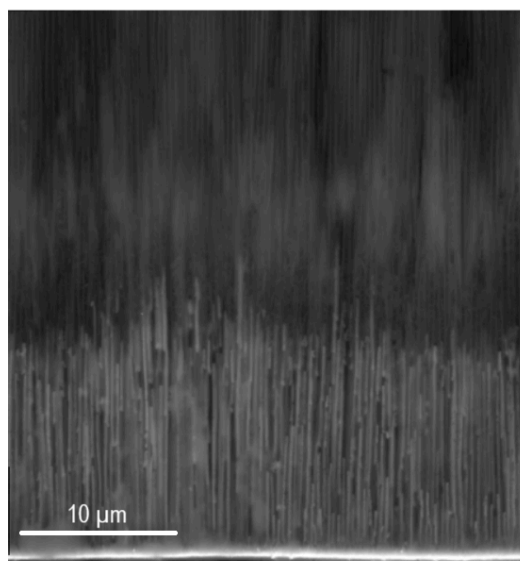
Source: França et al. (2023).

# 4 RESULTS AND DISCUSSION OF THE EMI SE RESULTS OVER THE TESTED SYSTEMS

The mechanism behind the measure of the electromagnetic interference shielding effectiveness consists as shown in section 2.5, where a vector network analyzer (briefly studied in section 2.4) is coupled with two rectangular waveguides with specifications described in section 2.3 acting in the microwave band X, for this experiment. The chamber is put between the waveguides and the samples of compounds (created in chapter 3) measured are fixed in it. To obtain a correct calibration, the shielding of the chamber is subtracted from the system sample plus chamber. It is then, obtained the S-parameters from the VNA and the total shield is calculated from equation 2.73 as described in section 2.6.2.

4.1 YTTRIUM IRON GARNET

Figure 15 shows the S-parameter obtained from the measure of the YIG, Figure 15A) shows the real part of S12, 15B) shows the imaginary part of S_{12}, 15C) shows the real part of S_{11} and 15D) shows the imaginary part of S_{11} from these parameters can be calculated the total shield. Often, for a good shielding effect, the square modulus of S_{12}(or S_{21}) has to be small, this do not occur on YIG, so it is plausible to expect a small shield, in fact, YIG is an insulator as described in section 2.2.2, what makes it a poor shield.

Figure 16 shows the total shield of YIG (remind that the total shield of the chamber is subtracted from the sample+chamber), the negative aspect on the shield represents that the system YIG+chamber is less effective than the chamber alone as a shielding material.

Figure 15 - S-Parameters of YIG. A)The real part of the S_{12} parameter, B)The imaginary part of S_{12}, C)The real part of S_{11}, D)The imaginary part of S_{11}.
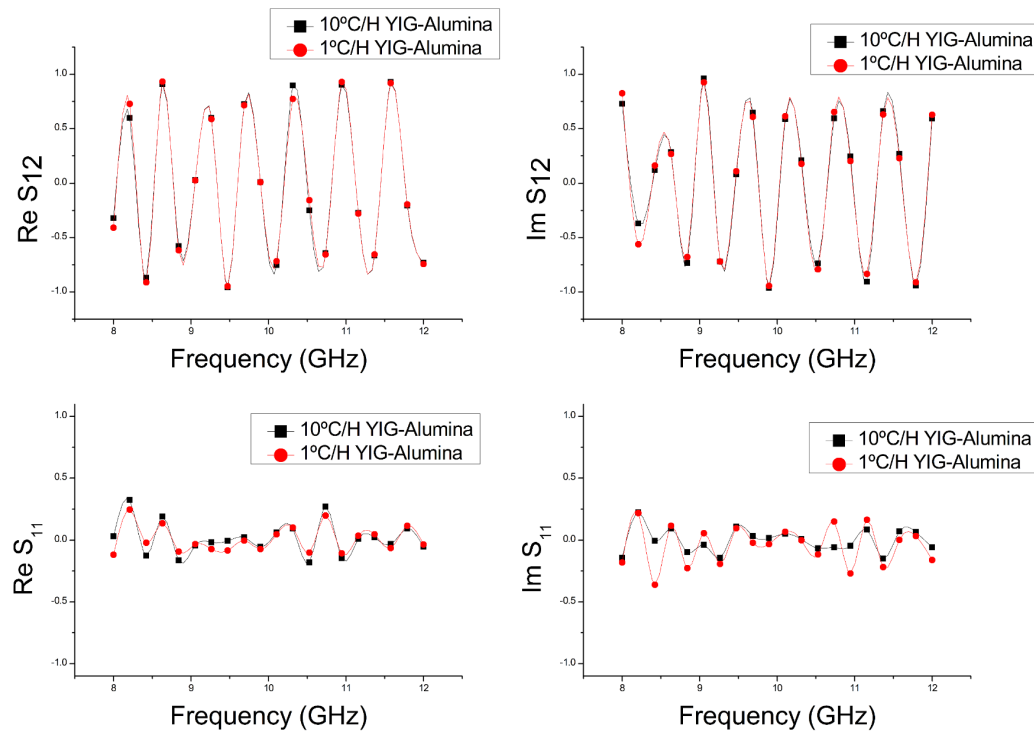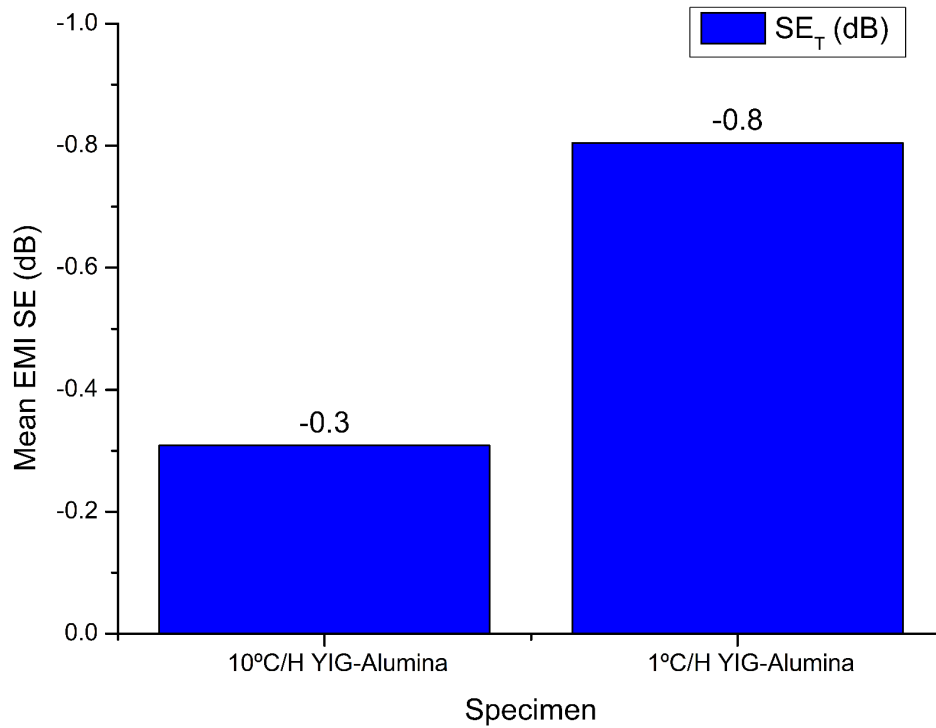

Source: The author.

Figure 16 - Total shield of YIG.
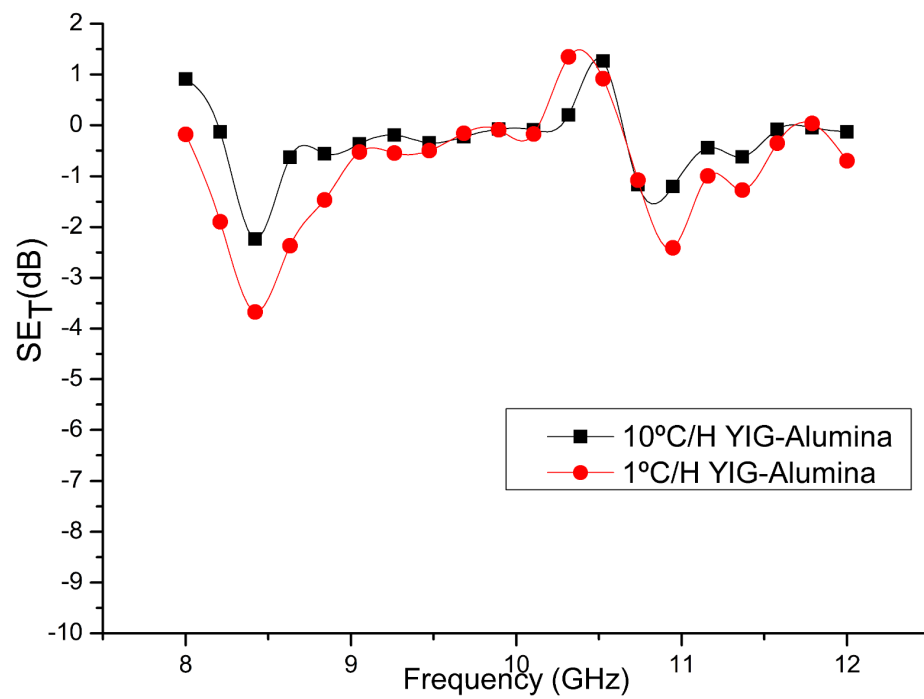
Source: The author.

Figure 17 - The mean shield of YIG.

Source: The author.

Figure 17 enforces this characteristic by showing the negative mean of the shield of YIG. This aspect was also found by Zaini *et al.* (2022) and corroborates the fact that YIG has an uncountable shield that is small enough to be undetected over the precision of the experiment (The shield of YIG is smaller than the shield of the chamber).

4.2 BACTERIAL CELLULOSE

To measure the bacterial cellulose acquired on section 3.2, the scheme described on section 2.5 was used, and the S-parameters obtained can be seen in Figure 18 for the BC-OVEN, and Figure 21 for the BC-LYO. Figure 18A shows the real part of the S_{11} parameter, while Figure 18B shows the imaginary part of S_{11}. Figure 18C shows the real part of the S_{21} parameter, while Figure 18D shows the imaginary part of S_{21} of the samples that went to the oven. The same occurs with Figure 21. Figure 21A shows the real part of the S_{11} parameter, while Figure 21B shows the imaginary part of S_{11}. Figure 21C shows the real part of the S_{21} parameter, while Figure 21D shows the imaginary part of S_{21} for the lyophilized samples.

Figure 18 - S-Parameters of BC - OVEN compounds. A)Real part of S_{11}. B)Imaginary part of S_{11}. C)Real part of S_{21}. D)Imaginary part of S_{21}.
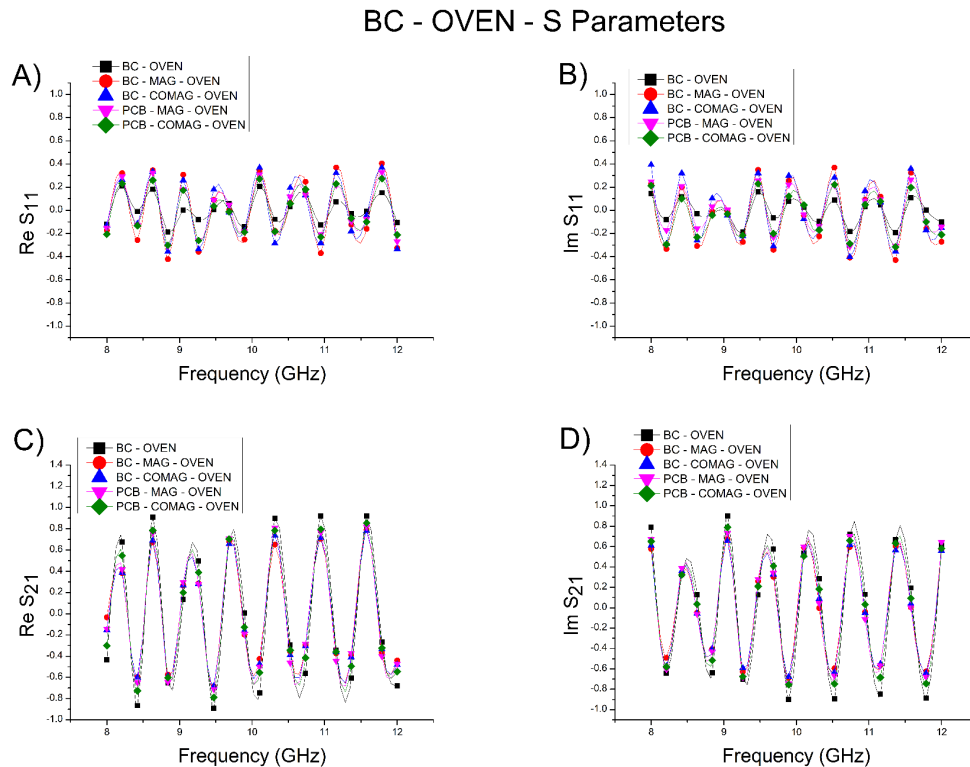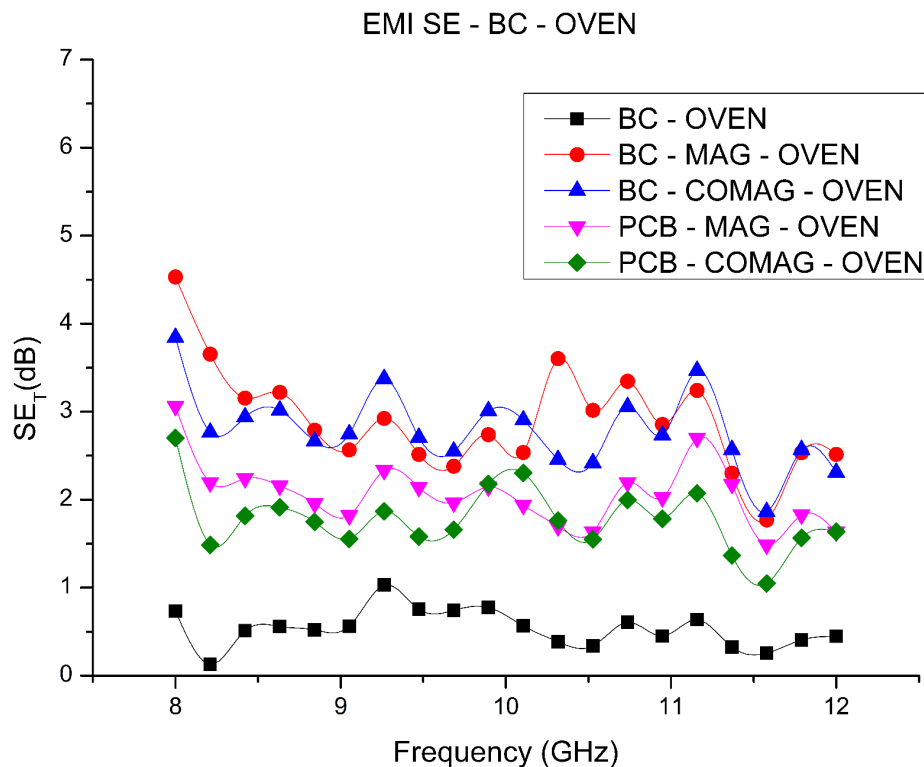

Source: The author.

As seen on Figure 19 and Figure 20, BC-OVEN with a thickness of 0.3 mm, exhibits small shielding characteristics. At its highest, it achieves a shielding effectiveness of 1 dB at 9.3 GHz, providing fable protection against electromagnetic

interference. Conversely, its smallest value is recorded at 0.1 dB, but at a slightly lower frequency of 8.2 GHz. On average, BC-OVEN maintains a mean shielding effectiveness of 0.5 dB, displaying insufficient and unreliable performance. The standard deviation of 0.2 dB suggests a level of consistency in its shielding capabilities, making BC-OVEN a material that is lacking competences for applications demanding electromagnetic shielding.

Meanwhile, BC-MAG-OVEN, boasting a thickness of 1.1 mm, proves to be a more robust contender in the domain of electromagnetic shielding. At its peak, it achieves an moderate, shielding effectiveness of 4.5 dB at 8.0 GHz, demonstrating a higher capacity to thwart electromagnetic interference, being the peak value for the samples studied. At its lowest, BC-MAG-OVEN maintains a respectable 1.8 dB at 11.6 GHz. The material exhibits a mean shielding effectiveness of 2.9 dB, attesting to its overall efficacy. With a standard deviation of 0.6 dB, BC-MAG-OVEN displays a degree of consistency on the measure.

Figure 19 - Total shielding effectiveness of BC - OVEN.

Source: The author.

The upcoming specimens were evaluated, resulting in the BC-COMAG-OVEN with a thickness of 0.3 mm within the higher value of 3.8 dB at 8.0 GHz and the smallest value of 1.9 dB at 11.6 GHz, a mean value of 2.8 dB with 0.4 dB of standard deviation. PBC-MAG-OVEN with thickness of 1.0 mm, higher value of 3.1 dB at 8.0 GHz and smallest value of 1.5 dB at 11.6 GHz,with a mean value of 2.1 dB with 0.4 dB of standard deviation, and finally PBC-COMAG-OVEN with thickness of 0.9 mm, higher value of 2.7 dB at 8.0 GHz, smallest value of 1.0 dB at 11.6 GHz and mean value of 1.8 dB with 0.4 dB of standard deviation.

Figure 20 - Mean EMI SE for the BC-OVEN compounds.
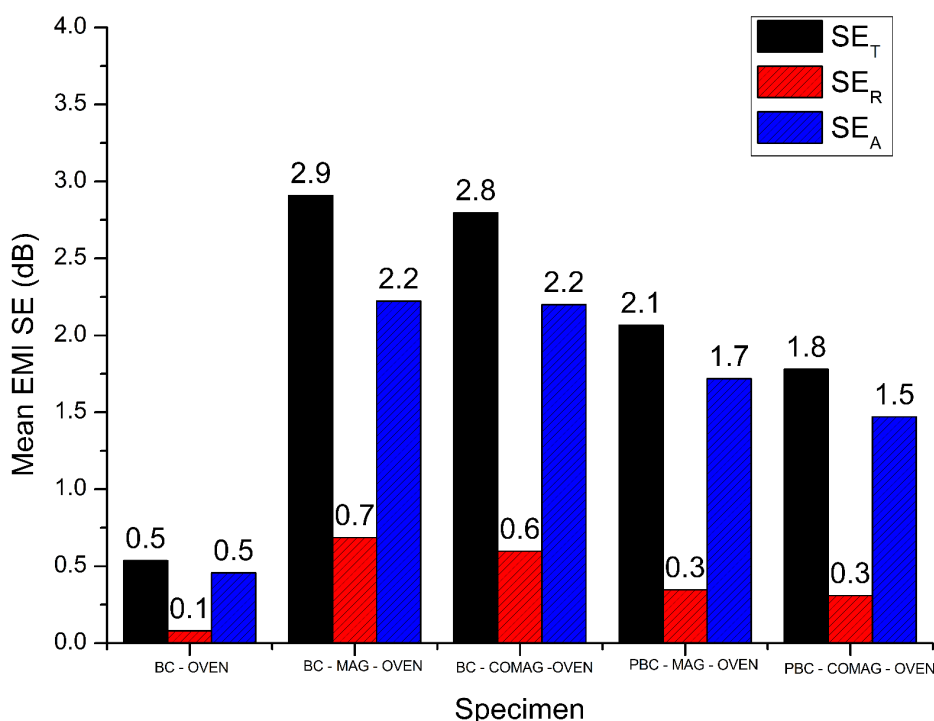
Source: The author.

As seen on Figure 22 and Figure 23, BC-LYO, with thickness of 0.4 mm, did not represent a very pleasant result when compared with BC-OVEN, depicting a maximum shielding of 1.6 dB around 10.3 GHz, mean shielding of 0.4 dB with standard deviation of 0.4 dB and small values of 0.0 dB around 11.6 GHz, representing a similar characteristic as the obtained from BC-OVEN, with small shielding.

However, BC-MAG-LYO, with thickness of 0.9 mm, represented the summit of shielding for the samples containing bacterial cellulose, its summit represented a

peak of 5.7 dB on frequencies around 8.0 GHz, a mean shielding of 4.5 dB and a standard deviation of 0.6 dB, with small values of 3.4 dB around 11.6 GHz.

Figure 21 - S-Parameters of BC - LYO compounds. A)Real part of S_{11}. B)Imaginary part of S_{11}. C)Real part of S_{21}. D)Imaginary part of S_{21}.
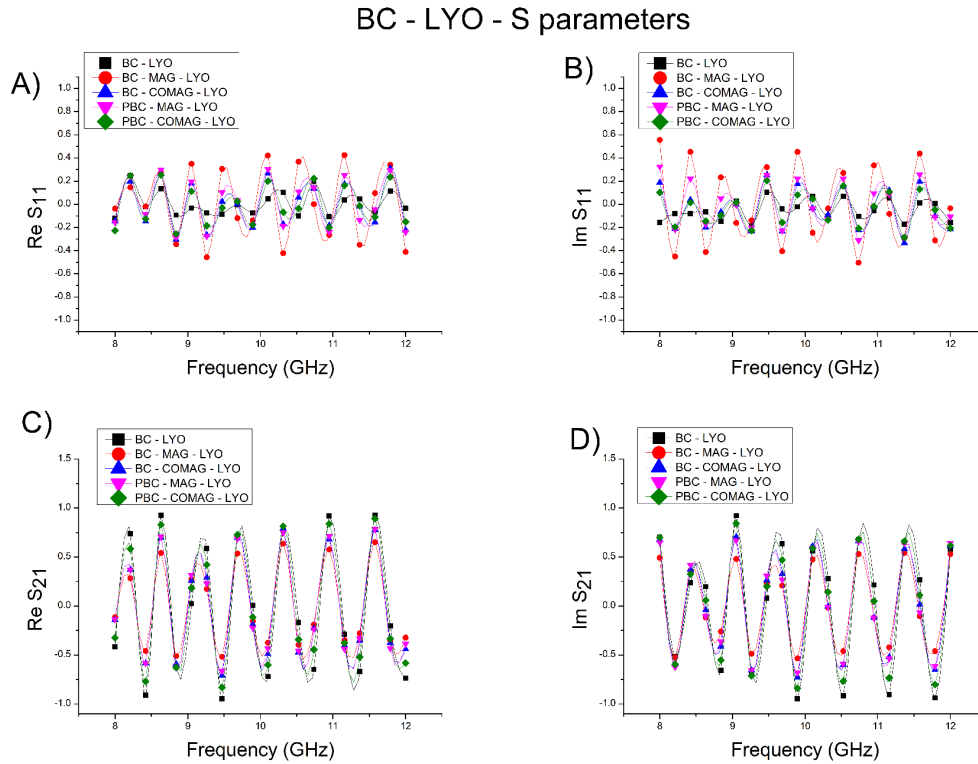
Source: The author.

The remaining specimen showed similar shielding performance as their BC-OVEN equivalent. BC-COMAG-LYO, with thickness of 1.6 mm, showed at frequencies of 11.1 GHz a higher shielding of 3.5 dB, meanwhile at frequencies of 10.3 , it depicted small shielding of 1.9 dB, with a mean value of 2.5 dB and standard deviation of 0.4 dB. PBC-MAG-LYO, with thickness of 2.1 mm, had a mean shielding of 2.6 dB, with higher shielding values of 3.4 dB at 8.0 GHz and smallest shielding values of 1.8 dB around 11.6 GHz, and its standard deviation of 0.3 dB. Finally PBC-COMAG-LYO, with thickness of 3.1 mm, obtained a maximum shielding of 2.1 dB for frequencies around 8.0 GHz, a smallest shielding of 0.6 dB around 11.6 GHz, and a mean shielding of 1.3 dB with standard deviation of 0.3 dB.

Figure 22 - Total shielding effectiveness of the BC-LYO compounds.

EMI SE - BC - LYO
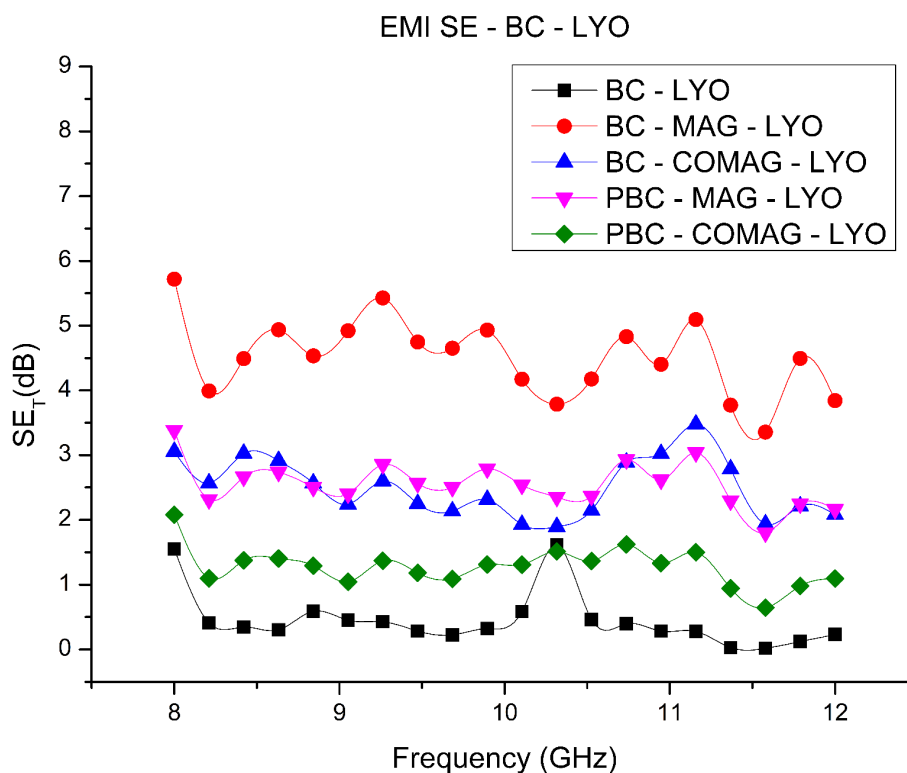
Source: The author.

Bacterial cellulose does not depict a strong EMI shielding potential, nonetheless, the shielding over thickness, as shown on Table 04, and the fact that high percentage of shielding for bacterial cellulose is due absorption, as the fact that BC is resistant of temperature changes and its malleable properties, can represent a possible use for bacterial cellulose as a material built for multiple-layered compounds as a membrane or subtract that can be used for shielding.

Figure 23 - Mean EMI SE of the BC-LYO compounds.
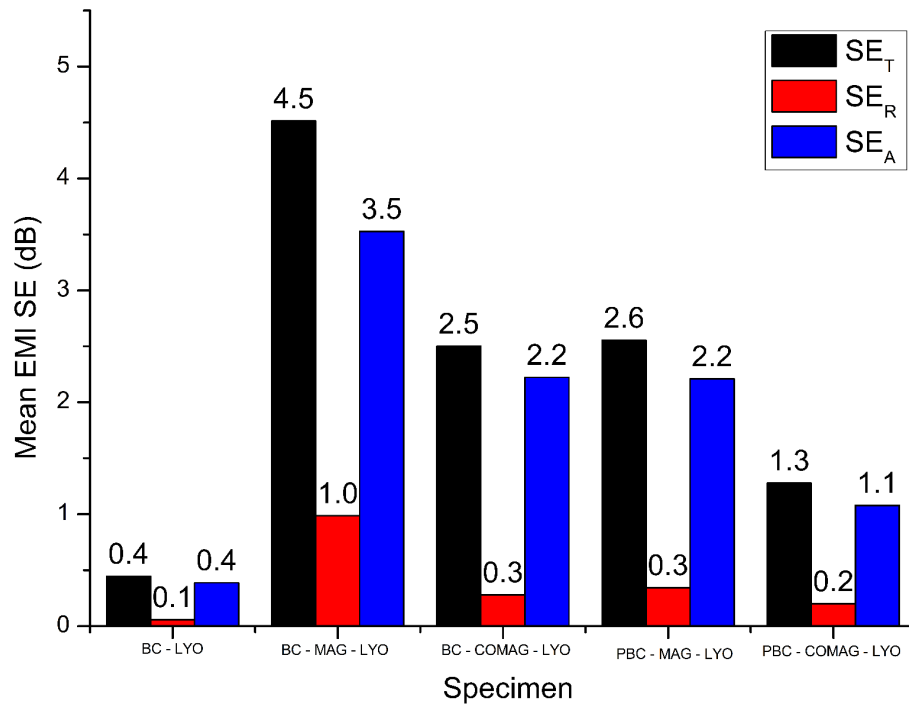
Source: The author.

Table 4 - Comparative values of cellulose/leather-like compounds.

Material	MXene/ BC	MXene/ Leather	CNT/BC-BP	MWCNT@ Fe3O4/CMC	BC - MAG - LYO	BC- COMAG-OVEN
EMI SE(dB)	41.0	30.1	24.0	0.23	5.7	3.8
Thickness (mm)	0.015	19	0.036	0.028	0.9	0.3
EMI SE/ Thickness (dB/mm)	2733	1.6	667	8.2	6.3	12.7
Frequency (GHz).	8-12	8.2-12.4	5.8-8.2	8-12	8-12	8-12

Source: Produced by the author.

MXene/BC: Luo, S. *et al.* (2023).

Mexene/Leather: Xing *et al.* (2023).

CNT/BC-BP: Fan *et al* (2022).

MWCNT@Fe$_3$O$_4$/CMC: Dai *et al.* (2024).

BC - MAG - LYO; BC - COMAG - OVEN: The author.

4.3 Fe$_3$O$_4$/NITROGEN-DOPED REDUCED GRAPHENE OXIDE AEROGEL

To study the shielding for the graphene oxide compounds was necessary to measure the S-Parameters of the compounds. Figure 24 shows the S-Parameters measured by the method described in section 2.5 for the compounds acquired in section 3.3. Figure 24 A) is the real part of S_{12}, B) is the imaginary part of S_{12}, C) is the imaginary part of S_{11}, and D) is the imaginary part of S_{11}.

Figure 24 - The S-Parameters of the graphene oxide compounds. A)Real of S_{12}. B)Imaginary of S_{12}. C)Real of S_{11}. D)Imaginary of S_{11}.
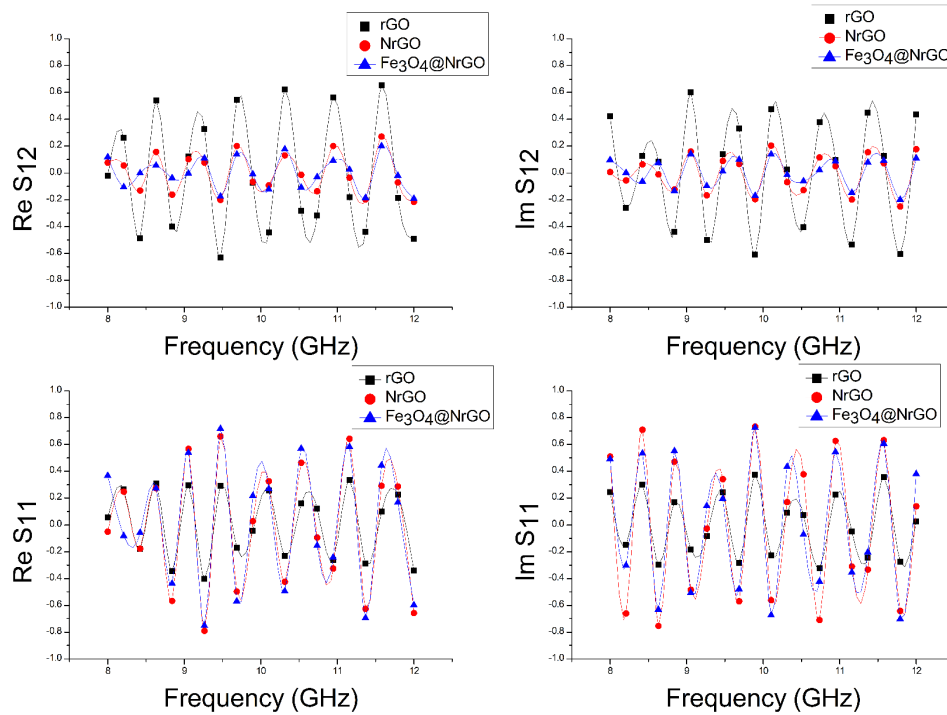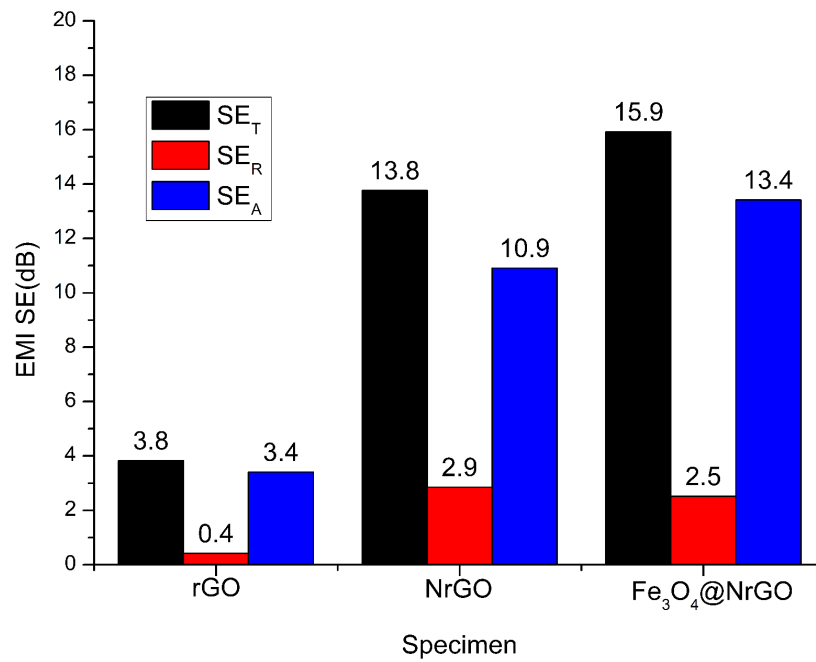

Source: The author.

The analysis of EMI SE revealed notable variations in performance across different materials and frequencies. rGO exhibited the highest EMI SE of 6.4dB around 8GHz, while its lowest value was 2.8dB at 8.6GHz. The average EMI SE for rGO was determined to be 3.8 dB, with a standard deviation of 0.9dB,indicating relatively consistent performance.

Figure 25 - Total shielding effectiveness of the graphene oxide compounds.
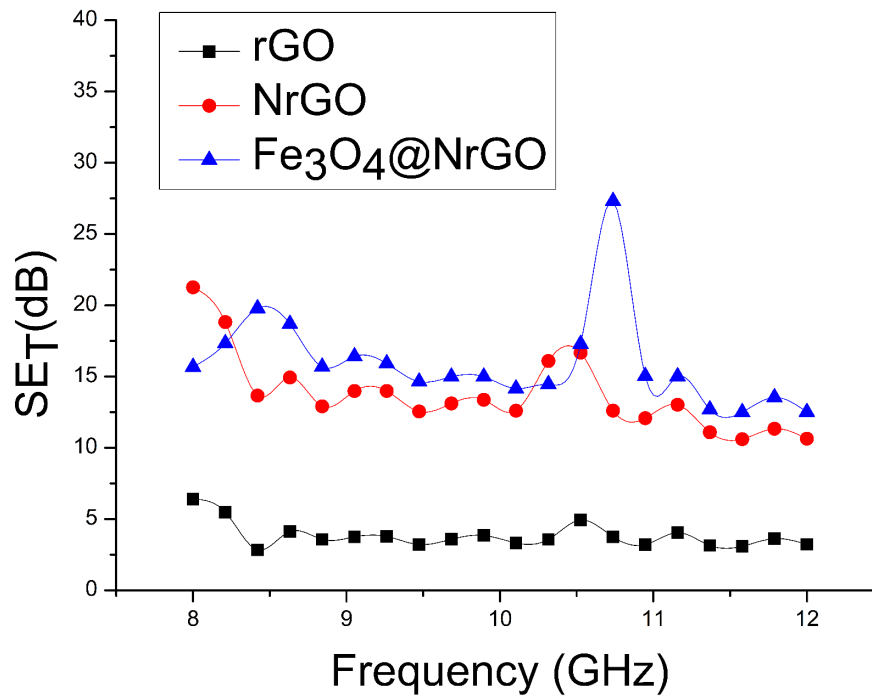
Source: The author.

Figure 26 - The mean EMI SE of the graphene oxide compounds.

Source: The author.

In contrast, the NrGO played a significant role in the shielding process, showcasing a peak SE of 21.3 dB at 8 GHz. However, its SE dropped to 10.6 dB at 12 GHz. The mean EMI SE for the NrGO was calculated as 13.8 dB, accompanied by a standard deviation of 2.7 dB, signifying a moderate level of variability.

Table 5 - Comparative shielding values for graphene-like materials.

Material	rGO/Cu foam.	SrGO	rGO& Fe3O4	NrGO/ WPU	rGO	NrGO	Fe3O4@ NrGO
EMI SE (dB).	32.6	22.5	13.4	28.3	6.4	21.3	27.3
Thickness (mm).	5	5	1	-	0.1	0.1	0.1
EMI SE/ Thickness (dB/mm).	6.5	4.5	13.4	-	64	213	273
Frequenc y (GHz).	8.2-12.5	1-18	8.2	9.0	8.0	8.0	10.7

Source: Produced by the author.

rGO/Cu foam: Yan *et al.* (2022).

SrGO: Das,P., Deoghare and Maity (2022).

rGO&Fe_3O_4: Liu, Y. *et al.* (2019).

NrGO/WPU: Tian *et al.* (2017).

rGO, NrGO and Fe_3O_4@NrGO: The author.

Turning attention to the Fe_3O_4@NrGO, their EMI SE values demonstrated distinct behavior. Specifically, the SE was recorded as 27.3 dB at frequencies around 10.7 GHz, while at 11.6 GHz, the SE was 12.5 dB. The collective performance of Fe_3O_4@NrGO yielded a mean SE of 15.9 dB, accompanied by a standard deviation of 3.3 dB, highlighting the variability in their EMI SE.

Figure 25 and Figure 26 show the dependence of the EMI SE with respect to the frequency on the X-Band. As mentioned above, the rGO has a wide below mean of EMI SE, while the NrGO has a substantial increase in its value. Meanwhile the Fe_3O_4@NrGO has also a significant boost on the EMI SE value and being able to

perform commercially on frequencies around 10.7 GHz, due its EMI SE peak of 27.3 dB.

Table 05 shows a comparative analysis of a few values of EMI SE for graphene like composites. The mean values for the NrGO and Fe_3O_4@NrGO found in this article are comparable with the literature. Fe_3O_4@NrGO has potential commercial applications for frequencies around 10.7 GHz.

4.4 COBALT NANOWIRES

To evaluate the process of electromagnetic (EM) shielding of cobalt nanowires produced in section 3.4, a crucial step was to measure the complex values of the S-parameters, as depicted in Figure 27. The S-parameters provide information about the behavior of the electromagnetic waves when they interact with the cobalt nanowire shield.

Figure 27 - The S-Parameters from the cobalt nanowire compounds. 27 A) Real part of S_{21}. 27 B) Imaginary part of S_{21}. C)Real part of S_{11}. D)Real part of S_{11}.
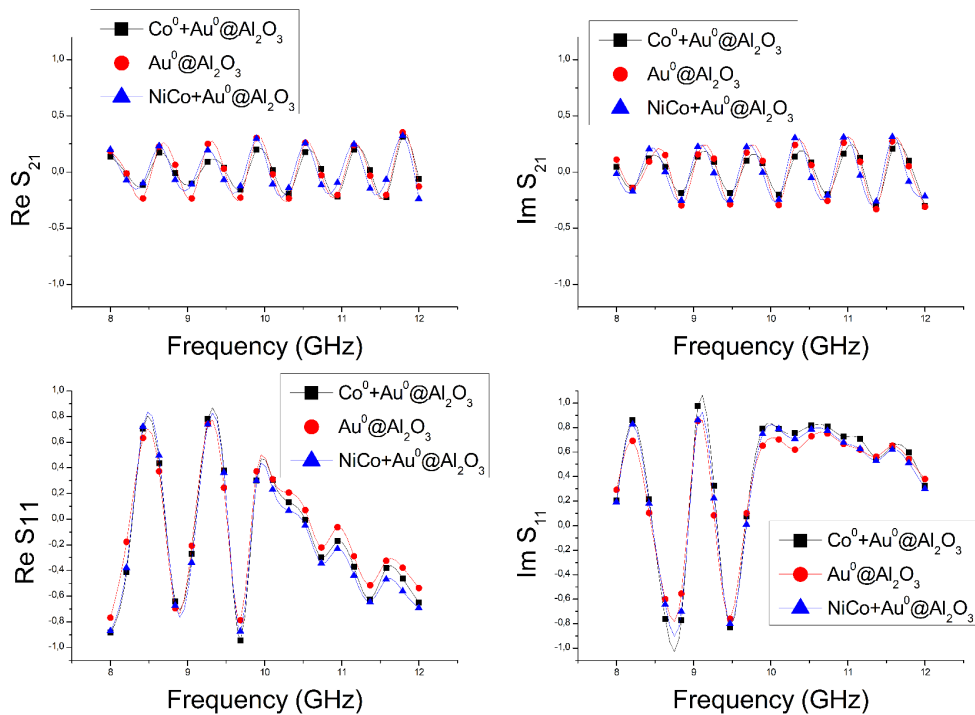
Source: The author.

In Figure 27 A and Figure 27 B, the S-parameters were measured for the reflected wave, which represents the electromagnetic wave reflected by the cobalt nanowires deposited on the alumina membrane grown up the gold layer. Figure 27 C and 27 D, on the other hand, shows the S-parameters for the transmitted wave, which represents the electromagnetic wave that passes through the cobalt nanowire shield. This measurement helps in assessing how effective the nanowire shield is in blocking or attenuating the transmitted wave.

Figure 28 -Total shielding effectiveness of the cobalt compounds.
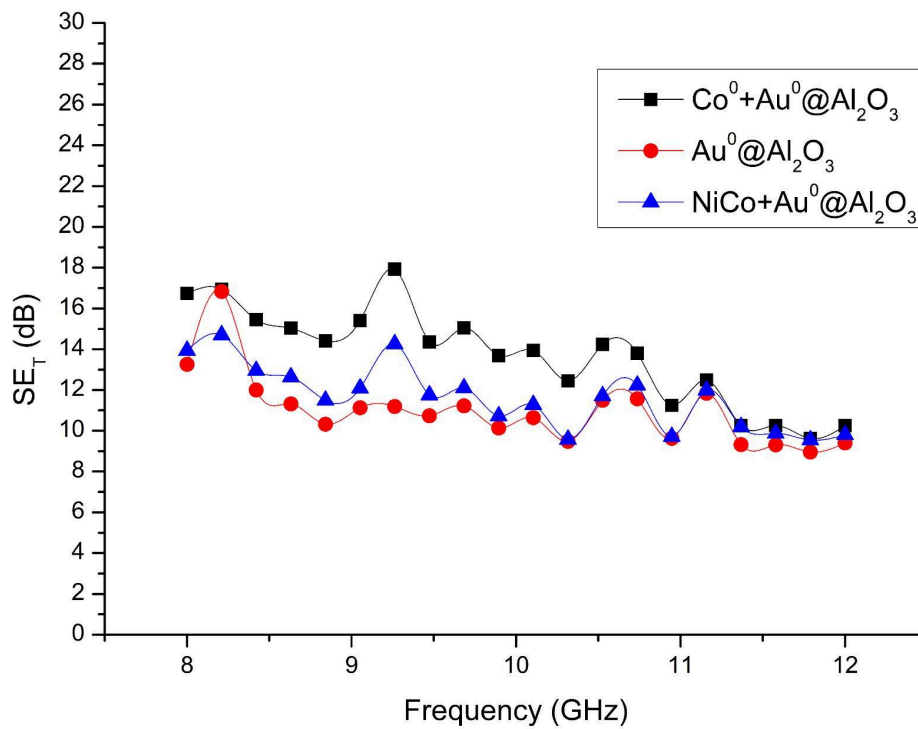
Source: The author.

As shown in Figure 28 and Figure 29, the values given for the SE_T found the summit (highest value) of 17.9 dB on frequencies around 9.3 GHz for the cobalt, while the lowest value was 9.6 dB found at 11.8 GHz, and the mean value was given as 13.7 dB with a standard deviation of 2.4 dB.

Figure 29 - The mean shielding of the cobalt nanowire compounds.
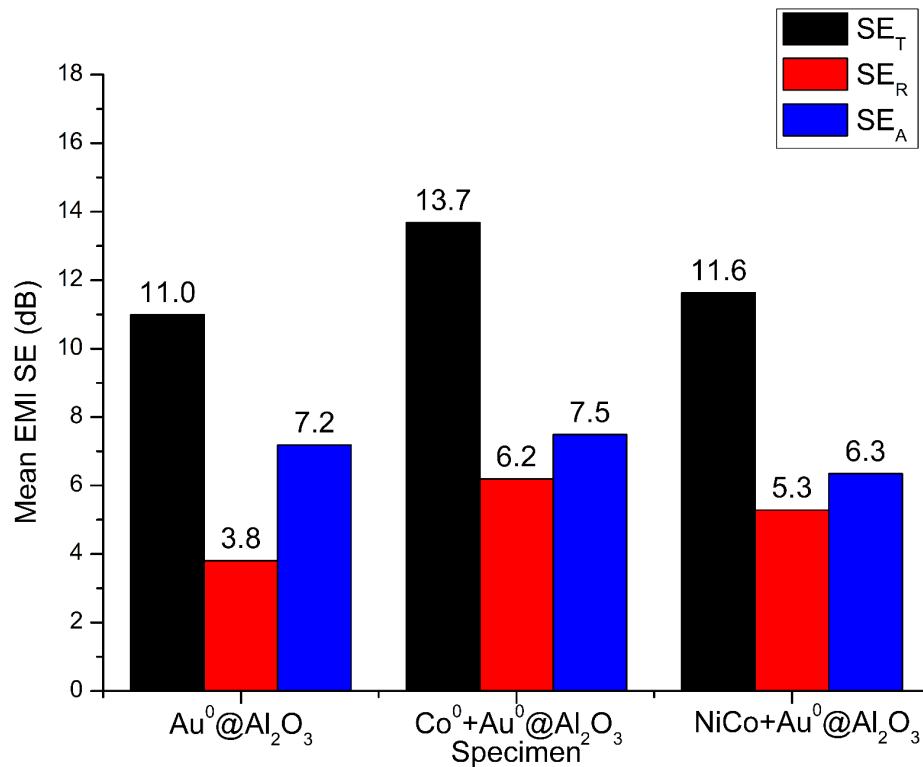
Source: The author.

The gold membrane itself was partially fundamental to the shielding process, given a higher value of 16.8 dB at 8.2 GHz, while its lowest value was 9.0 dB at 11.8 GHz, within a mean EMI SE of 11.0 dB and a standard deviation of 1.8 dB. For the NiCo nanowires the values found were 14.7 dB for frequencies around 8.2 GHz, 9.5 dB at 11.8 GHz, and a mean value of 11.6 dB within a standard deviation of 1.6 dB.

The shielding can be acquired from an absorption or a reflection process. Figure 29, shows graphically the average part of the shielding process that is generated due an absorption or reflection process. It is evident that more than 50% of the shielding process occurs primarily due absorption. As said early, the blindage becomes useful for devices around 20 dB, which implies that the cobalt nanowires have a moderated blindage.

4.5 IRON NANOWIRES

Figure 30 shows the sketch parameters obtained from the iron nanowire samples produced in section 3.5, Figure 30 A shows the real part of S_{12}, 30 B shows the imaginary part of S_{12}, while 30 C shows the real part of S_{11} and 30 D shows the imaginary part of S_{11}.

Figure 31 shows the dependance of the total EMI SE from the above mentioned compounds over the frequency on the microwave X-Band. The compounds have thickness of $65\,\mu m$, and their shape was made a circular membrane of alumina, to grow the nanowires.

Figure 30 - The S-Parameters of the iron nanowires. A)Real part of S_{12}. B)Imaginary part of S_{12}. C)Real part of S_{11}. D)Imaginary part of S_{11}.
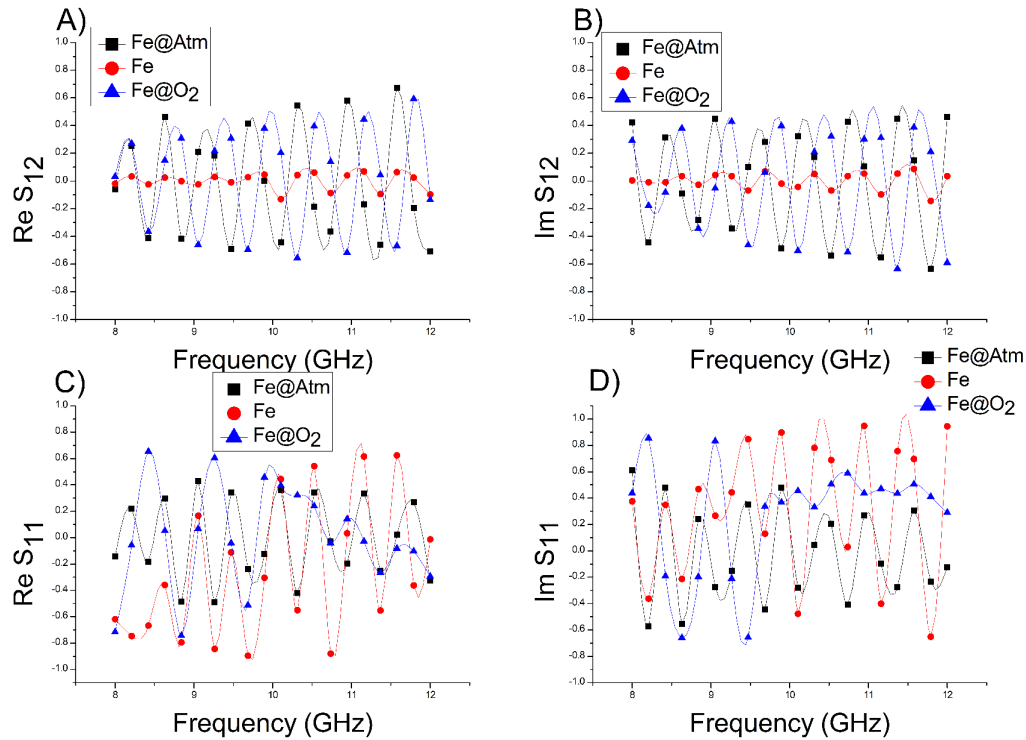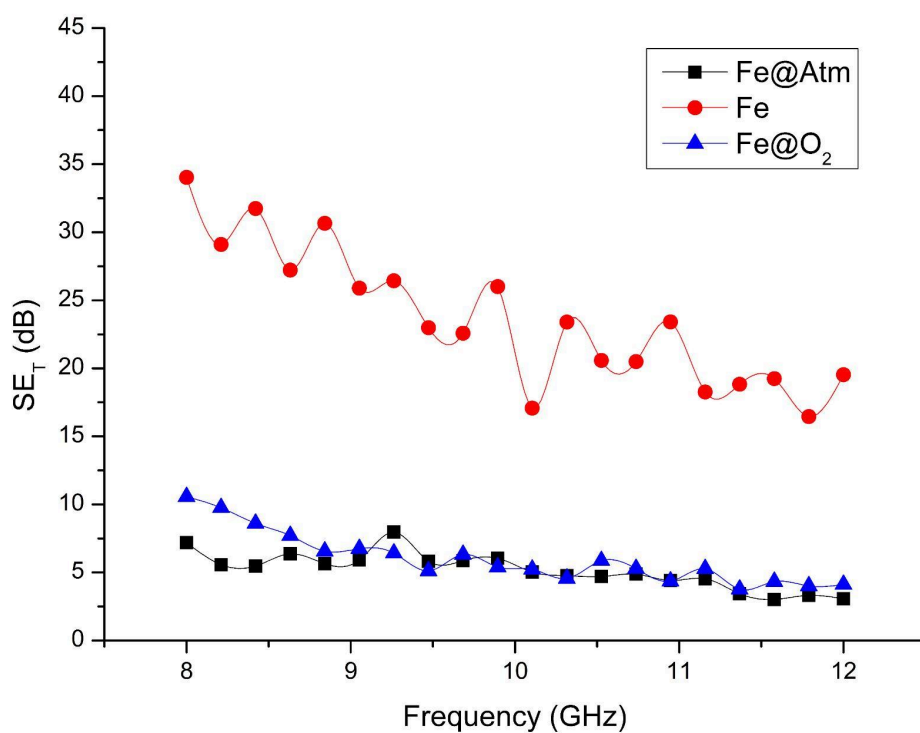

Source: The author.

The metallic nanowires of iron have depicted the far up results for shielding. Of the three measurements, the most significant part of the process occurred due the absorption processes on the media, being more significant on the Fe@Atm, where the described process was accountable for more than 80% of the shielding.

Meanwhile on modulus, the absorption process was accountable for 17.4 dB on the FeNWs.
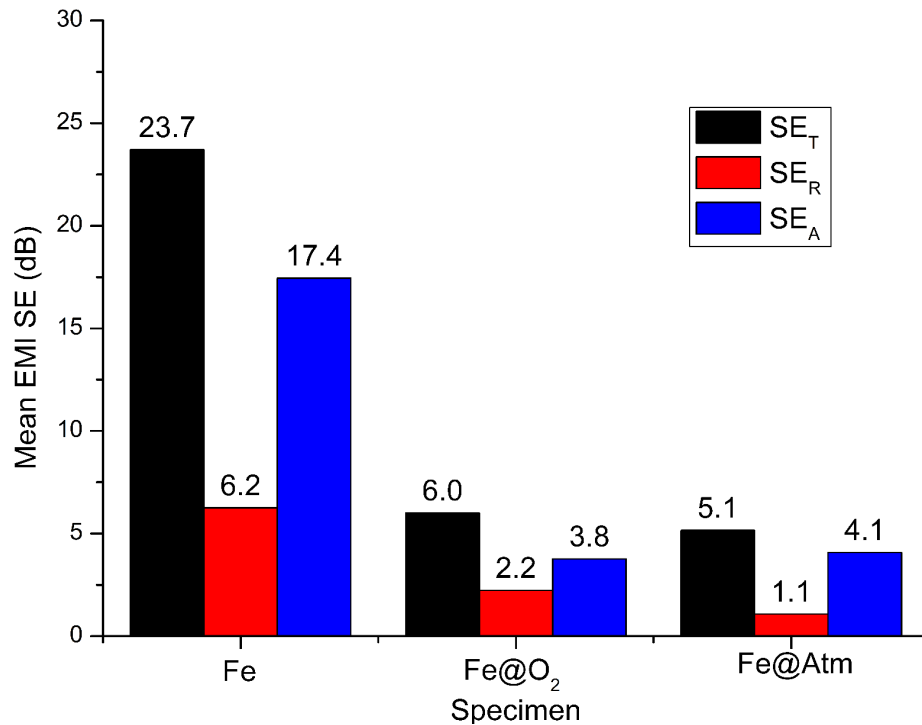
Figure 31 - Total shielding effectiveness of the iron nanowires.

Source: The author.

The total shielding process, as seen in Figure 31 have mean values of 23.7dB, 6.0 dB and 5.1 dB, with standard deviations of 5.1 dB, 1.9 dB and 1.3 dB for the Fe, Fe@O_2 and Fe@Atm, respectively, while a summit of 34.0 dB at 8 GHz, 10.6 dB at 8 GHz and 7.9 dB at 9.3 GHz.

Figure 32 - The mean shield of the iron nanowires.

Source: The author.

Figure 32 shows how the mean EMI SE drops when the FeNWs are oxidized over the atmosphere and over oxygen gas. It is depicted that the upcoming oxygen gas datains a bigger fraction of the absorbed shielding process, making its total EMI SE be slightly above when compared to the one oxidized on the atmosphere. The retaining properties of absorption gives a small advantage for the $Fe@O_2$ compounds. This shows that when in contact with the atmosphere, the shielding process of the FeNWs can be impaired over the performance.

Comparative values found on Table 06, gave the maximum shielding values for each set of experiments. The nanowires, indeed, have a similar shielding effect from the others. The growth of the nanowires usually increases with the thickness of the media where the waves permeate. The reduction on shielding within the growth of the nanowires indicates that the Co nanowires slightly ameliorate the reflection-absorption mechanism when compared to the NiCo nanowires. Meanwhile the total shielding effect of iron nanowires is slightly superior.

Table 6 - Comparative values of total shielding for nanowire compounds.

Material.	CuNW	PEDOT: PSS & AgNW	V2O5 NW	SiC/Fe@ CNT	NiCo NW	CoNW	FeNW
EMI SE(dB).	35	68.8	34	70	14.7	17.9	34
Thickness (mm).	0.21	0.025	6.0	1.8	0.092	0.093	0.065
EMI SE/ Thickness. (dB/mm).	166.7	2750	5.7	38.9	159.8	192.5	523.1
Frequency (GHz).	8-12	8-12	8-12	8.2-12.4	8.2	9.3	8.0

Source: Produced by the author

CuNW: Al-Saleh, Gelves and Sundararaj (2011).

PEDOT:PSS&AgNW: Liu, G. *et al*. (2023).

V_2O_5 NW: Narayanan, Unni and Surendran (2021).

SiC/Fe@CNT: Mei *et al*. (2019).

NiCo NW; Co NW; Fe NW: The author

5 CONCLUSION

This work searched for practical means of achieving sufficiently high shields for electromagnetic pollution, bearing in mind the characterization and the media where this pollution occurs. It found a feeble and almost nonaccountable shield for the yttrium-iron garnet, an small shielding of 5.7 dB for bacterial cellulose, and a moderate shielding for the cobalt nanowire of 17.9 dB, also was depicted a high shield of 27.3 dB for the nitrogen doped graphene oxide with Fe_3O_4 and 34.0 dB for the iron nanowires. The compounds studied in this work gave the following results for shielding:

Yttrium-iron garnet:
1. Due to its insulating properties, YIG did not present a significant shielding, small enough to be small then the precision of the experiment.
2. YIG can not be used as a potential shielding for the problem of electromagnetic pollution.

Bacterial cellulose:
1. Bacterial cellulose generates a small shielding that can not be used as a commercial device for shielding by itself.
2. Because of its environment-friendly behavior and high EMI SE per millimeter, bacterial cellulose can be used as a substrate for developing multi-layered materials that can be applied for shielding processes.

Fe_3O_4@NrGO:
1. The results for Fe_3O_4@NrGO had shown an exceptionally strong shielding effect, and can be used as a commercial shielding material.
2. The ratio shielding due absorption/total shielding of Fe_3O_4@NrGO implies that it is an environment-friendly material for blocking the second kind of electromagnetic pollution.

CoNW:
1. Cobalt nanowires have shown a great shielding effect that can be used for commercial applications if the layer thickness grows.
2. Due to its conductive properties CoNW can be used in electric devices to protect them from electromagnetic interference.

FeNW:

1. Exhibited the best values for shielding and shielding per thickness in this work, which makes it the ideal material for protecting electronic devices, humans and the environment from electromagnetic interference.

2. Presented a high absorption ratio, which makes it a potential compound for shielding the second kind of EMI pollution.

Overall: This work proposed five compounds for solving the problem of electromagnetic interference pollution by measuring their shielding effectiveness and found out that three of them (Fe_3O_4@NrGO, CoNW and FeNW) represent a potential commercial compound as shielding material, being FeNW the summit of this work's applications.

6 OUTLOOK.

- Conduct experiments over a wide range of frequencies beyond the X band of the MW spectrum.
- Characterization of the bacterial cellulose.
- Start making multiple layered systems to acquire an improvement on the shielding effect.
- Archive higher patamar on EMI SE by making more thick probes.
- Make the experimental set depending on the temperature.
- Try new kinds of membranes for substrates (polycarbonates, BC, etc…)
- Measure Permittivity (ϵ) and Permeability (μ) depending on the frequency.
- Measure the skin depth.
- Measure the electrical conductivity depending on the frequency.
- Measure new systems (for example rotating the experiment in multiple angles or measure).
- Measure new compounds (from silver and copper nanowires, to more bio supportive ones, like organic metals/semiconductors, etc…).

REFERENCES

AL-SALEH, M.; GELVES, G.; SUNDARARAJ, U. Copper nanowire/polystyrene nanocomposites: Lower percolation threshold and higher EMI shielding. **Composites Part A: Applied Science and Manufacturing**. v. 42, n. 1, p. 92-97, 2011.

AHMAD, H. *et al.* Graphene and Fe2O3 filled composites for mitigation of electromagnetic pollution and protection of electronic appliances. **Composites Science and Technology Journal**. v. 240, n. 110097, 2023.

AKRAM, S. *et al.* Recent advances in electromagnetic interference (EMI) shielding textiles: A comprehensive review. **Journal of Synthetic Metals**. v. 294, n. 117305, 2023.

BOYCE, W.; DIPRIMA, R.; MAEDE, D. **Elementary Differential Equations**.12. ed., Hoboken: John Wiley & Sons, 2022.

CARVALHO, A. *et al*. Binder-free ultrathin pellets of nanocomposites based on Fe3O4@nitrogen-doped reduced graphene oxide aerogel for electromagnetic interference shielding. **Journal of Alloys and Compounds**, v. 978, n. 173329, 2024.

CASTRO-LOPES, S. **Influência da modulação por composição sobre as propriedades microestruturais e magnéticas de nanofios de ni/cu**. Tese de doutorado (Doutorado em ciência de materiais), Universidade Federal de Pernambuco, 2023.

CHANTHIWONG, M. *et al.* Controlling the processing of co-precipitated magnetic bacterial cellulose/iron oxide nanocomposites. **Mater. Des.** v. 196, n. 109148, 2020.

CHHETRI, S. *et al.* Synergistic effect of Fe3O4 anchored N-doped rGO hybrid on mechanical, thermal and electromagnetic shielding properties of epoxy composites. **Composites Part B: Engineering**. v. 166, p. 371-381, 2019.

COLLIN, R. **Foundations for Microwave Engineering**. 2. ed., Hoboken: John Wiley & Sons, 2001.

COSTA, S. *et al.* Production Of Bacterial Cellulose By Gluconacetobacter Hansenii Using Corn Steep Liquor As Nutrient Sources. **Front. Microbiol**. v. 8, n. 2017, p. 1 - 12, 2017.

DAI, Y. *et al*. Electromagnetic interference shielding of flexible carboxymethyl cellulose/MWCNT@Fe3O4 composite film with ultralow reflection loss. v. 257, n. 128604, 2024.

DAS, M.; SETHY, P.; SUNDARAY, B. EMI shielding performance of graphene oxide reinforced polyaniline/polystyrene solution cast thin films. **Synthetic Metals Journal**. v. 296, n.117369, 2023.

DAS, P.; DEOGHARE, A.; MAITY, S; Synergistically improved thermal stability and electromagnetic interference shielding effectiveness (EMI SE) of in-situ synthesized polyaniline/sulphur doped reduced graphene oxide (PANI/S-RGO) nanocomposites. **Ceramics International Journal**. v. 48, n. 8, p. 11031-11042, 2022.

ERDOGAN, N. *et al.* ITO/Au/ITO multilayer thin films on transparent polycarbonate with enhanced EMI shielding properties. **Current Applied Physics Journal**. v. 20, i. 4, p. 489-497, 2020.

FAN, M. *et al*. Sustainable bacterial cellulose reinforced carbon nanotube buckypaper and its multifunctionality for electromagnetic interference shielding, Joule heating and humidity sensing. **Chemical Engineering Journal**. v. 441, n. 136103, 2022.

FENG, X. *et al.* Self-healing, EMI shielding, and antibacterial properties of recyclable cellulose liquid metal hydrogel sensor. **Carbohydrate Polymers Journal**. v. 311, n. 120786, 2023.

FRANÇA, E. *et al*. Effect of pH and precursor solution on the microstructural properties and ferromagnetic resonance of nickel nanowires. **Materials Letters**. v. 342, 134360, 2023.

GALDINO, S. *et al*. Evaluation of the potential of bacterial cellulose in the treatment of oily waters. **Chemical Engineering Transactions**, v. 74, p. 313–318, 2019.

GRIFFITHS, D. **Introduction to Electrodynamics**. 4. ed., Cambridge: Cambridge University Press, 2017.

HA, H. *et al*. Mini review of synthesis strategies of silver nanowires and their applications. **Journal of Colloid and Interface Science Communications**. v. 50, n. 100663, 2022.

HAYATI, L. *et al.* Ferromagnetic Resonance of Y3Fe5O12 Nanowires. **IEEE Magnetics Letters**. v. 9, n. 4106204, p. 1-4, 2018.

HESTRIN, S.; SCHRAMM, M. Synthesis of cellulose by Acetobacterxylinum: II. Preparation of freeze - dried cells capable of polymerized glucose to cellulose. **Biochem.J.** v. 58, p. 345–352, 1954.

HSU, C. *et al.* Nanowires Properties and Applications: A Review Study. **South African Journal of Chemical Engineering**. v. 46, 286-311, 2023.

HUNGUND, S.; GUPTA, S. Improved production of bacterial cellulose from Gluconacetobacter persimmonis GH-2. **J. Microb. Biochem. Technol**, v. 2, n. 05, p. 127-133, 2010.

IEEE. IEEE Standard Method for Measuring the Effectiveness of Electromagnetic Shielding Enclosures. **IEEE Std 299-2006 (Revision of IEEE Std 299-1997)**. p 1-52, 2007.

JACKSON, J. **Classical Electrodynamics**. 3. ed., Hoboken: John Wiley & Sons, 1998.

JI, H. *et al*. Lightweight and Flexible Electrospun Polymer Nanofiber/Metal Nanoparticle Hybrid Membrane for High-Performance Electromagnetic Interference Shielding. **NPG Asia Materials**. v. 10, p. 749–760, 2018.

KHAN, A. **Microwave Engineering: Concepts and Fundamentals**. Boca Raton: CRC Press, 2014.

LERICI, L. *et al*. Fe-doped Al2O3 nanoplatforms as efficient and recyclable photocatalyst for the dyes remediation. **Journal of Photochemistry and Photobiology A: Chemistry**. v. 426, n. 113733, 2022.

LI, R. *et al*. Fe NWs/CNT/PUS composite constructed rigid-flexible coupling 3D porous structure with highly linear response and large strain for strain sensor. **Sensors and Actuators A: Physical**. v. 353, n. 114211, 2023.

LIPIEC, W.; SOBCZAK, J.; TRZECIAK, A. The influence of rotational motion of Fe and Fe/Cu nanowires on their activity when applied as co-catalysts in aerobic oxidation of acroleine catalyzed by N-hydroxyphtalimide. **Applied Catalysis A: General**. v. 506, p. 8-13, 2015.

LIU G, *et al.* PEDOT:PSS and AgNW synergistically contributed high electromagnetic shielding performance for polyurethane-based composite coating. **Composites Part A: Applied Science and Manufacturing**. v. 175, n. 107769, 2023.

LIU, X. *et al.* Fabrication and electromagnetic interference shielding effectiveness of carbon nanotube reinforced carbon fiber/pyrolytic carbon composites. Carbon Journal, v. 68, p. 501-510, 2014.

LIU, Y. *et al.* Anisotropic thermal conductivity and electromagnetic interference shielding of epoxy nanocomposites based on magnetic driving reduced graphene oxide@Fe3O4. **Composites Science and Technology**. v. 174, p. 1-10, 2019.

LUO, H. *et al.* Synthesis and analysis of the magnetic properties of YIG by means of sol–gel and spark plasma sintering. **Journal of Magnetism and Magnetic Materials**. v. 589, n. 171595, 2024.

LUO, S. *et al.* Reinforcing and toughening bacterial cellulose/MXene films assisted by interfacial multiple cross-linking for electromagnetic interference shielding and photothermal response. **Journal of Colloid and Interface Science**. v. 652b, p. 1645-1652, 2023.

MARCUVITZ, N. **Waveguide Handbook**. Edison: IET, 1986.

MARIAPPAN, P. Effects of electromagnetic interference on the functional usage of medical equipment by 2G/3G/4G cellular phones: A review. **Journal of Advanced Research**. v. 7, p. 727-738, 2016.

MATHUR, P.; RAMAN S. Electromagnetic Interference (EMI): Measurement and Reduction Techniques. **Journal of Electronic Materials**. v. 49, n. 5, 2020.

MAXWELL, J. A Dynamical theory of the electromagnetic field. **Philosophical Transactions of the Royal Society of London**, v. 155, p. 459–512. 1864.

MEI, H. *et al*. SiC encapsulated Fe@CNT ultra-high absorptive shielding material for high temperature resistant EMI shielding. **Ceramics International Journal**. v. 45, n. 14, p. 17144-17151, 2019.

MERIZGUI, T. *et al.* High Content Silver/Zinc Oxide Nanoparticle and Cobalt Nanowire in Caryota Urens Fibre-Epoxy Composites for Enhanced Microwave Shielding. **Journal of Magnetism and Magnetic Materials**. v. 536, n. 168118, 2021.

MOORE, G. Cramming more components onto integrated circuits. **Electronics magazine**. v. 38, n. 8, 1965.

NAN, Z. *et al*. Flexible nanocomposite conductors for electromagnetic interference shielding. **Nano-Micro Lett**, v. 15, n. 172, 2023.

NARAYANAN, A.; UNNI, K. SURENDRAN, K. Aerogels of V2O5 nanowires reinforced by polyaniline for electromagnetic interference shielding. **Chemical Engineering Journal**. v. 408, n. 127239, 2021.

NEWZOO, Newzoo Global Mobile Market Report, **Newzoo**. p. 18, 2021.

OLUMUREWA, K. *et al*. Effect of incorporating graphene oxide in ZnS and study of the thermistor applications of ZnS-RGO film. **Applied Surface Science Advances**. v. 13, n. 100370, 2023.

PAI, A. *et al.* Recent Progress in Electromagnetic Interference Shielding Performance of Porous Polymer Nanocomposites—A Review. **MDPI Energy Journal**. v. 15, n. 3901, 2022.

PESSOA, P. *et al.*, Fabrication of elongated YIG nanostructures by the sol-gel method supported on alumina membranes. **J Sol-Gel Sci Technol**. v. 108, p. 458-465, 2023.

POZAR, D. **Microwave engineering**. 4. ed., Hoboken: John Wiley & Sons, 2012.

QI, F. *et al*. Robust Ti3C2Tx MXene/starch derived carbon foam composites for superior EMI shielding and thermal insulation. **Materials Today Physics Journal**. v. 21, n. 100512, 2021.

RYU, S. *et al.* Absorption-dominant, low reflection EMI shielding materials with integrated metal mesh/TPU/CIP composite. **Chemical Engineering Journal**. v. 428, n. 131167, 2022.

SUN, Y. *et al.* Metal-grade laminated nanofiber films with outstanding EMI shielding performances and high-temperature resistance. **Colloids and Surfaces A: Physicochemical and Engineering Aspects**. v. 680, n. 132701, 2024.

SALLES T. R. *et al*. Magnetic nanocrystalline cellulose: Azithromycin adsorption and in vitro biological activity against melanoma cells. **J. Polym. Environ.** v. 30, p. 2695–2713, 2022.

SVELTO, O. **Principles of Lasers**. 5. ed., New York: Springer, 2012.

TAKAHARI, K. *et al.* First Report of Electromagnetic Interference Between Percutaneous Ventricular Assist Device and Implantable Cardioverter-Defibrillator. **JACC Case Rep**. v. 21, n. 101981, 2023.

TIAN, K. *et al*. N-doped reduced graphene oxide/waterborne polyurethane composites prepared by in situ chemical reduction of graphene oxide. **Composites Part A: Applied Science and Manufacturing**. v. 94, p. 41-49, 2017.

ULABY, F. **Microwave Radar and Radiometric Remote Sensing**. Ann Arbor: University of Michigan Press, 2014.

VERMA, R. *et al*. A review on MXene and its composites for electromagnetic interference (EMI) shielding applications. **Carbon Journal**. v. 208, p. 170-190, 2023.

VU, M. *et al*. Hybrid shell of MXene and reduced graphene oxide assembled on PMMA bead core towards tunable thermoconductive and EMI shielding nanocomposites. **Composites Part A: Applied Science and Manufacturing**. v. 149, n. 106574, 2021.

WANG, G. *et al.* Flexible and transparent silver nanowires/biopolymer film for high-efficient electromagnetic interference shielding. **Journal of Colloid and Interface Science**. v. 607, p. 89-99, 2022.

WANG, H. *et al.* Review on Shielding Mechanism and Structural Design of Electromagnetic Interference Shielding Composites. **Macromolecular Materials and Engineering Journal**. v. 306, n. 2100032, 2021.

WANG, X. *et al*. Green EMI shielding: Dielectric/magnetic "genes" and design philosophy. **Carbon Journal**. v. 206, p. 124-141, 2023.

WANG, Y. *et al*. Multilayer-Structured Ni-Co-Fe-P/Polyaniline/Polyimide Composite Fabric for Robust Electromagnetic Shielding with Low Reflection Characteristics. **Chemical Engineering Journal**. v. 380, n. 122553, 2020.

WANG, Y. H.; LI, C. Highly effective EMI shielding composites for 5G Ka-band frequencies. **Applied Materials Today Journal**. v. 36, n. 102041, 2024.

WANASINGHE, D.; ASLANI, F. A Review on Recent Advancement of Electromagnetic Interference Shielding Novel Metallic Materials and Processes. **Composites Part B: Engineering**. v. 176, n. 107207, 2019.

WANASINGHE, D.; ASLANI, F.; MA, G. Electromagnetic Shielding Properties of Carbon Fibre Reinforced Cementitious Composites. **Construction and Building Materials Journal**. v. 260, n. 120439, 2020.

WORLD HEALTH ORGANIZATION. Radiation: Electromagnetic fields. **World Health Organization**, 2016. Available in:

https://www.who.int/news-room/questions-and-answers/item/radiation-electromagnetic-fields. Accessed on 16 jan. 2024.

WORLD HEALTH ORGANIZATION. Radiation: Ionizing radiation. **World Health Organization**, 2020. Available in: https://www.who.int/news-room/questions-and-answers/item/radiation-ionizing-radiation. Accessed on 19 jan. 2024.

XING, W. *et al*. Preparation and properties of multifunctional polyurethane synthetic leather nanocomposites. **Composites Part A: Applied Science and Manufacturing**. v. 169, n. 107534, 2023.

XU, H. *et al.* Free-standing reduced graphene oxide/carboxymethylcellulose-polyaniline (RGO/CMC-PANI) hybrid film electrode for high-performance asymmetric supercapacitor device. **International Journal of Biological Macromolecules**. v. 236, n. 123934, 2023.

YAN, A. *et al*. RGO reinforced Cu foam with enhanced mechanical and electromagnetic shielding properties. **Journal of Materials Research and Technology**. v. 21, p.2965-2975.

YAZDI, M. *et al*. Preparation and EMI shielding performance of epoxy/non-metallic conductive fillers nano-composites. **Progress in Organic Coatings Journal**. v. 145, n. 105674, 2020.

ZAINI, N. *et al*. Structural, morphological and shielding effectiveness properties of Yttrium Iron Garnet/Epoxy composites at X-Band frequency prepared via solid state reaction method. **Materials Today: Proceedings**. v. 51, p. 1426-1431, 2022.

ZANGWILL, A. **Modern electrodynamics**. Cambridge: Cambridge University Press, 2012.

ZHANG, N. *et al*. Lightweight and Flexible Ni-Co Alloy Nanoparticle-Coated Electrospun Polymer Nanofiber Hybrid Membranes for High-Performance

Electromagnetic Interference Shielding. **Journal of Alloys and Compounds**. v. 784, p. 244-255, 2019

ANNEX A - SCIENTIFIC PRODUCTION

Published papers:

CARVALHO, A.; **SANTOS, A.**; CABRAL, D.; OLIVEIRA, D.; ASSIS, L; FRANÇA, E.; QUIRINO, F.; CASTRO-LOPES, S.; COSTA, O.; PADRÓN-HERNÁNDEZ, E. Binder-free ultrathin pellets of nanocomposites based on Fe3O4@nitrogen-doped reduced graphene oxide aerogel for electromagnetic interference shielding. **J**ournal of Alloys and Compounds, v. 978, n. 173329, 2024.

Papers in preparation or submitted (all the names are subjected to changes):

CASTRO-LOPES, S.; OLIVEIRA, D.; **SANTOS, A**.; FRANÇA, E.; CARVALHO, A.; ABRÃO, J.; PADRÓN HERNÁNDEZ, E. Metallic electrodeposited cobalt nanowires in alumina membrane for electromagnetic interference shielding effectiveness.

FRANÇA, E.; **SANTOS, A**.; ASSIS, L.; CASTRO-LOPES, S.; OLIVEIRA, D.; CARVALHO, A.; PESSOA, P.; PADRÓN HERNÁNDEZ, E. Exploring Electrodeposited Iron and Iron Oxide Nanostructures on Porous Alumina Membrane for Enhanced EMI Shielding.

PESSOA, P.; ASSIS, K.; ABRÃO, J.; **SANTOS, A.**; RODRIGUES, A.; PADRÓN-HERNÁNDEZ, E. Study of the magnetic properties and shielding effectiveness of yttrium iron garnet elongated structures fabricated inside alumina membranes by a sol-gel method.

SOUZA, T.; **SANTOS, A**.; PADRÓN HERNÁNDEZ, E. Thin bacterial cellulose for environment harmless electromagnetic interference shielding effectiveness.

Works present in conferences:

Figure 33 - Presented conferences.

Source: The author

Patent applications:

"Nanofios metálicos eletrodepositados em membranas de alumina: abordagem promissora para blindagem contra interferência eletromagnética.".

Número do Pedido - INPI: BR 10 2023 026972 9.

Data do Depósito: 20/12/2023.

Hora do Depósito: 15:29h (horário de Brasília).